ORIGINAL ARTICLE

Miriplatin-loaded liposome, as a novel mitophagy inducer, suppresses pancreatic cancer proliferation through blocking POLG and TFAM-mediated mtDNA replication

Xiaowei Wang[a,b], Mengyan Wang[a], Meilian Cai[a], Rongguang Shao[a], Guimin Xia[b,*], Wuli Zhao[a,*]

[a]State Key Laboratory of Respiratory Health and Multimorbidity, Key Laboratory of Antibiotic Bioengineering, Ministry of Health, Laboratory of Oncology, Institute of Medicinal Biotechnology, Chinese Academy of Medical Sciences and Peking Union Medical College, Beijing 100050, China
[b]Pharmaceutics Department, Institute of Medicinal Biotechnology, Chinese Academy of Medical Sciences and Peking Union Medical College, Beijing 100050, China

Abstract Pancreatic cancer is a more aggressive and refractory malignancy. Resistance and toxicity limit drug efficacy. Herein, we report a lower toxic and higher effective miriplatin (MPt)-loaded liposome, LMPt, exhibiting totally different anti-cancer mechanism from previously reported platinum agents. Both in gemcitabine (GEM)-resistant/sensitive (GEM-R/S) pancreatic cancer cells, LMPt exhibits prominent anti-cancer activity, led by faster cellular entry-induced larger accumulation of MPt. The level of caveolin-1 (Cav-1) determines entry rate and switch of entry pathways of LMPt, indicating a novel role of Cav-1 in nanoparticle entry. After endosome−lysosome processing, in unchanged metabolite, MPt is released and targets mitochondria to enhance binding of mitochondria protease LONP1 with POLG and TFAM, to degrade POLG and TFAM. Then, via PINK1−Parkin axis, mitophagy is induced by POLG and TFAM degradation-initiated mitochondrial DNA (mtDNA) replication blocking. Additionally, POLG and TFAM are identified as novel prognostic markers of pancreatic cancer, and mtDNA replication-induced mitophagy blocking mediates their pro-cancer activity. Our findings reveal that the target of this liposomal platinum agent is mitochondria but not DNA (target of most platinum agents), and totally distinct

---

*Corresponding authors.
E-mail addresses: wenlyzh@imb.pumc.edu.cn (Wuli Zhao), xiaguimin@imb.pumc.edu.cn (Guimin Xia).

mechanism of MPt and other formulations of MPt. Self-assembly offers LMPt special efficacy and mechanisms. Prominent action and characteristic mechanism make LMPt a promising cancer candidate.

1. Introduction

Pancreatic cancer is one of the most refractory and aggressive digestive system cancer. With its increasing incidence and poor prognosis, pancreatic cancer has a high mortality rate worldwide (4.5% in 2020) and a poor 5-year survival rate (< 10%) (WHO GLOBOCAN, 2020)[1], making it a serious health burden. However, because of the inconspicuous symptoms, rapid progression, and lack of diagnostic markers, most pancreatic cancers are unresectable at diagnosis, making chemotherapy a vital treatment option for pancreatic cancer[2,3]. Gemcitabine (GEM) is the standard first-line drug for pancreatic cancer treatment[2]. However, primary and secondary resistance limits the clinical application of GEM[2]. In addition to GEM, oxaliplatin (OXA) is listed as the first-line treatment for patients with locally advanced pancreatic cancer in the National Comprehensive Cancer Network guidelines of the USA[4]. However, the lack of specificity for *in vivo* distribution, neurotoxicity, and myelosuppressive toxicity greatly limits OXA application in pancreatic cancer treatment. Therefore, safer and more effective agents are required to improve the treatment efficacy of pancreatic cancer.

Liposomes are one of the most effective drug delivery systems for cancer therapy. Their unique structure offers liposomes various advantages in tumor treatment, the most remarkable ones being increased efficacy, passive tumor targeting, lower toxicity, biocompatibility and biodegradability[5]. Specifically, after injection into the blood, liposomes can protect the encapsulated drug from physiological disruption and fast plasma clearance, contributing to prolonged half-life and thus strengthened therapeutic efficacy[6,7]. Furthermore, during *in vivo* circulation, liposomes preferentially accumulate in tumor tissue *via* the enhanced permeability and retention effect, called passive targeting of liposomes[8], and thus decrease the nonselective toxicity of anti-cancer drug application. Moreover, upon reaching the tumor cells, the phospholipid membranous structure, resembling natural cell membranes, promotes efficient cellular uptake by forming excellent interactions between liposomes and cell membranes[6,9]. Additionally, liposomes can co-load different types of biomolecules such as genes and proteins to expand these biomolecules application in photodynamic therapy and immunotherapy of tumors[5,10−16].

Platinum agents are classical anti-cancer drugs with broad anti-cancer spectrum and potential anti-cancer abilities[17,18], but side effects such as kidney toxicity and neurotoxicity limit their application. Liposome formulation of platinum agents may be beneficial for overcoming these drawbacks[19]. Several platinum-based liposomes have been constructed and assayed in lab or clinical trials, such as SPI-077 (liposomal formulation of cisplatin)[20], Lipoplatin (liposomal formulation of cisplatin)[21], Lipoxal (liposomal formulation of OXA)[22], Aroplatin (liposomal formulation of NDDP), albumin-bound nanoparticle and platinum ultrasmall dots encapsulated nanoparticle[18,23]. But so far, there are no platinum-based liposomes or nanoparticles approved[24]. Inadequate *in vivo* drug release and unclear mechanism of action may hinder their further pharmaceutical development[25].

As the third-generation platinum agent, miriplatin (MPt) (Supporting Information Fig. S1A) is designed and synthesized for local administration of transarterial chemoembolization for unresectable hepatocellular carcinoma[26,27]. MPt is poorly soluble in water and organic solvents[28], and its sole clinical formulation is the MPt/lipiodol suspension (Miripla, Dainippon Sumitomo Pharma, Osaka, Japan). Although MPt suspension is effective in transarterial chemoembolization treatment for hepatocellular carcinoma, this formulation cannot be used for intravenous administration. After careful analysis, we found that MPt, containing two long myristoyl chains, is highly lipophilic and structurally similar to phospholipids, forming phospholipid bilayers in liposomes (Fig. S1A)[29]. Thus, we hypothesized that the two long myristoyl chains of MPt would encapsulate into phospholipid layers, forming liposomes[30,31]. Accordingly, our team prepared a novel liposomal formulation of MPt:LMPt, also named lipomiriplatin (Fig. S1B)[29]. Pharmaceutical evaluations showed that LMPt possessed fine pharmaceutical characteristics, including favorable colloidal properties, high drug-loading capacity and robust stability (Fig. S1C and S1D)[29]. Considering that MPt is a structural analog of OXA[32,33], which is used for the treatment of pancreatic cancer, we wondered that if LMPt could be applied to the treatment of pancreatic cancer, employing the passive targeting ability of liposomal formulation to realize increased efficacy and reduced toxicity, which might be beneficial to overcome resistance. However, the therapeutic effect, as well as the expected action mechanism of LMPt on cancer has not been previously studied, which needs in-depth research.

In this study, we demonstrated that LMPt could exert potent anti-cancer activity in both GEM-resistant (GEM-R) and GEM-sensitive (GEM-S) pancreatic cancer cells. The endocytosis-induced increased accumulation of LMPt contributed to potent anti-cancer activity, and the level of caveolin-1 (Cav-1) allows for LMPt accumulation and determines the switch of entry pathways (caveolae or macropinocytosis), revealing a novel role of Cav-1. In mechanism exploration, we first proved that, instead of DNA as usually reported, the main target of this liposomal platinum agent, LMPt, is the mitochondria. In addition, we found that mitophagy mediated its anti-cancer activity. Based on these findings, we further clarified that the mtDNA-associated enzymes, DNA polymerase gamma (POLG) and Recombinant transcription factor A (TFAM), played a negative role in mitophagy in tumor cells, which has not yet been reported. These results uncover LMPt possessing a totally distinct mechanism from previously reported platinum agents, including MPt and other formulations of MPt.

2. Material and methods

2.1. Reagents

For LMPt preparation, DMPG (1,2-dimyristoyl-*sn*-glycero-3-phosphoglycerol, F0344), cholesterol (for injection, B41239) and mPEG$_{2000}$-DSPE (1, 2-distearoyl-*sn*-glycero-3-phosphoethanol amine-*N*-[amino (polyethylene glycol)-2000], B51152) were obtained from AVT (Shanghai, China). MPt was bought from Kunming Guiyan Pharmaceutical Company, Ltd. GEM and OXA were purchased from Cancer Hospital of the Chinese Academy of Medical Sciences (Beijing, China). Endocytosis inhibitors: cytochalasin D (CytoD, C102396), chlorpromazine (CPZ, C131611), genistein (G106673) were purchased from Aladdin (Shanghai, China); amiloride (A0080) and nystatin (IN0260) were purchased from Solarbio (Beijing, China). Autophagy inhibitors 3-methyladenine (3-MA, HY-19312) and Bafilomycin A1 (Baf-A1, HY-100558), endoplasmic reticulum (ER) stress inhibitors 4-phenylbutyric acid (4-PBA, HY-A0281) and tauroursodeoxycholate (TUDCA, HY-19696) were all bought from MedChemExpress (Shanghai, China). DiI (D-282), lipofectamine 2000 (11668019) and lipofectamine RNAiMAX (13778030) transfection reagent were purchased from Invitrogen (Waltham, MA, USA). 3-(4,5-Dimethyl-2-thiazolyl)-2,5-diphenyl-2*H* tetrazolium bromide (MTT) and sulforhodamine B (SRB) were purchased from Sigma−Aldrich (MO, USA).

For organelle labeling, early endosomes labeling reagent (CellLight Early Endosomes-GFP *BacMam 2.0*, C10586), late endosomes labeling reagent (CellLight Late Endosomes-GFP *BacMam 2.0*, C10588), lysosomes labeling reagent (CellLight Lysosomes-GFP *BacMam 2.0*, C10596) and mitochondria labeling reagent (CellLight Mitochondria-GFP *BacMam 2.0*, C10508) were obtained from Invitrogen (MA, USA). Mito-Tracker Red CMXRos (C1035) was purchased from Beyotime (Jiangsu, China). ER lumen labeling plasmids sfGFP-ER-5 was a gift from Michael Davidson (Addgene plasmid #56483).

Antibodies were as follows: anti-caveolin-1 (AF1231), anti-ATP7B (AF6264), anti-GSTP1 (AF7038), anti-IRE1α (AI601-1), anti-phospho-IRE1α (AF5842), anti-PINK1 (AF7755), anti-FEN1 (AF6885), anti-PCNA (AF1363), anti-Rad51 (AF7860), anti-ATF4 (AF2560) and anti-ATF6 (AF6243) antibodies were purchased from Beyotime (Jiangsu, China). Anti-H2AX (Ser139, 80312), anti-LC3B (3868), anti-Ubiquitin (3936), anti-POLG (13609), anti-TFAM (D5C8), anti-BiP (C50B12), anti-PERK (5683), anti-eIF2α (5324), anti-phospho-EIF2α (Ser51, 3398), anti-CHOP (5554), anti-SAPK/JNK (92527), anti-phospho-SAPK/JNK (9255s), anti-XBP-1s (12782s), anti-COXIV (3E11), and anti-GAPDH (D16H11) antibodies were purchased from Cell Signaling Technology (MA, USA). Anti-clathrin HC antibody (sc-12734) was purchased from Santa Cruz (California, USA). Anti-POLG2 antibody (10997-2-AP), anti-LONP1 antibody (66043-1-Ig) was bought from Proteintech (Rosemont, Maryland, USA). Anti-MRP2 (ab172630), anti-Parkin (phospho S101, ab73015) were purchased from Abcam (MA, USA). Anti-ATP7A (TA350995) was obtained from OriGene (Beijing, China). For secondary antibodies, Peroxidase-conjugated goat anti-mouse (ZB-2305) and goat anti-rabbit (ZB-2301) secondary antibodies were purchased from OriGene (Beijing, China). The fluorescent secondary antibodies, goat anti-rabbit IgG(H + L) highly cross-adsorbed secondary antibody (Alexa Fluor 633, A-21071), donkey anti-rabbit IgG(H + L) highly cross-adsorbed secondary antibody (Alexa Fluor 488, A-21206) were purchased from ThermoFisher (MA, USA).

Constructs: wild-type human caveolin-1 pCMV3 plasmid (HG11440-UT), human POLG pCMV3 plasmid (HG17306-UT), human POLG2 pCMV3 plasmid (HG19722-UT) and human TFAM pCMV3 plasmid (HG15937-NM), were purchased from Sino Biological (Beijing, China).

Small interfering RNA (siRNA): clathrin HC siRNA (h) (sc-35067) and caveolin-1 siRNA (h) (sc-29241) were purchased from Santa Cruz (California, USA). si-h-POLG_101 (siG000005428A-1−5) and si-h-TFAM_001 (siB144193812-1-5) were purchased from Ribobio (Guangzhou, China).

Primers used in this study were synthesized in Sangon Biotech (Shanghai, China):

Cav-1 forward, 5′-GCGGCCGCATGTCTGGGGGCAAATAC-3′,
Cav-1 reverse, 5′-GAATTCTTATATTTCTTTCTACAAGTTG-3′;
POLG forward, 5′-TGCAGTGAGGAGGAGGAGTT-3′,
POLG reverse, 5′-CCCAGGTAAGTGCCATAGAT-3′;
TFAM forward, 5′-TAAGACTGCAAGCAGCGAAG-3′,
TFAM reverse, 5′-TTCTCAGTTTCCCAGGTGCT-3′;
NADH dehydrogenase subunit 2 (*ND2*) forward, 5′-CCCTTACCACGCTACTCCTA-3′;
ND2 reverse, 5′-GGCGGGAGAAGTAGATTGAA-3′;
β-Actin forward, 5′-AGACGCAGGATGGCATGGG-3′,
β-Actin reverse, 5′-GAGACCTTCAACACCCCAGCC-3′.

2.2. Cells and animals

AsPC-1, BxPC-3, MIA-PaCa-2, PANC-1 and SU.86.86 human pancreatic cancer cells were obtained from the Institute of Basic Medical Sciences, Chinese Academy of Medical Sciences (Beijing, China) and cultured in RPMI-1640 or DMEM supplemented with 10% fetal bovine serum and 1% antibiotics in an incubator at 37 °C with 5% CO$_2$.

BALB/c nude mice (6−8 weeks old, 18−22 g) were purchased from SPF (Beijing, China). All care and handling of animals were complied with the ARRIVE (Animal Research: Reporting of *In Vivo* Experiments) guidelines and carried out in accordance with the National Research Council's Guide for the Care and Use of Laboratory Animals. All animal protocols were approved by the China Medical University Animal Care and Use Committee.

2.3. LMPt and fluorescence-labeled LMPt

LMPt was prepared by a thin-film dispersion technique using MPt and other conventional lipid materials (DMPG, cholesterol and mPEG$_{2000}$-DSPE) as previously described[29]. Fluorescence DiI labeled LMPt (DiI-LMPt) was prepared in the same way as LMPt except for adding 63 μg DiI (in a total ingredient molar ratio of 5%) into the organic solvent, and the stability was similar to LMPt. LMPt was dispersed as individual particles with spherical structure with size of 125.23 ± 5.23 nm, zeta potential of −57.87 ± 2.49 mV, drug-loading capacity of 19.04%, entrapment efficiency of 99%, robust storage stability at 2−10 °C for at least 3 years (Fig. S1C) and at 37 °C for least 14 days in cell culture medium (Fig. S1D).

2.4. Cell viability assay

MTT and SRB assay was used to analyze cellular viability[34]. For MTT assay, a total of 5000 cells per well were cultured in a 96-well plate. At the indicated incubation time points after the

addition of the tested drugs, the medium was replaced by 100 μL fresh medium containing 20 μL MTT solution (5 mg/mL) for each well. After additional 4 h incubation, the medium was discarded and 150 μL dimethylsulfoxide (DMSO) was added into each well to solubilize the converted formazan. Blank wells were set at the same time. The absorbance was read at 490 nm with a microplate reader (elx800, BioTek, USA). Survival (%) was calculated at each concentration, and the IC_{50} values were calculated by SigmaPlot. For SRB assay, cells were seeded in 6-well plates for adherence. Then the medium was changed to LMPt or OXA containing medium suspension for 48 h incubation. Then cells were fixed with 10% (*w/v*) trichloroacetic acid and stained with SRB for 30 min, after which the excess SRB was removed by washing with 1% (*v/v*) acetic acid. SRB staining was recorded by digital images and then dissolved in 10 mmol/L tris base solution for absorbance determination at 570 nm using a microplate reader for survival calculation.

2.5. Colony formation assay

Cell colony formation assay was performed with reference to the previously published article[35]. Briefly, 1000 cells were seeded in a 6-well plate and treated with different concentrations of LMPt or OXA for 12 h. Then, the previous medium was replaced with fresh medium. After continued incubation for 10 days, the cells were washed with PBS, fixed with 2% paraformaldehyde for 15 min at room temperature, stained with 0.1% crystal violet solution (C0121, Beyotime, Jiangsu, China) for 10 min and washed three times with sterile water. Digital images of the colonies in each well were obtained. Colonies were counted using ImageJ software (version 1.52a, National Institutes of Health, Bethesda, MD, USA) to calculate colony formation rate Eq. (1):

Colony formation (%) = (Number of colonies/Number of seeded cells) × 100   (1)

2.6. EdU proliferation assay

5-Ethynyl-2′-deoxyuridine (EdU) assay was used to evaluate cell DNA replication[35] using Cell-Light EdU Apollo488 *In Vitro* Kit (C10310-3, Ribobio, Guangzhou, China). Briefly, a total of 5×10^4 cells were seeded in a 24-well plate cell slide for adherence, followed with EdU assay according to the standard commercial protocols. Digital images of the cells were obtained under fluorescence microscope (IX73, Olympus, Japan) and the EdU positive rates were analyzed using ImageJ software.

2.7. In vivo antitumor efficacy and safety evaluation

An AsPC-1 mouse xenograft model was established by subcutaneously implanting 0.1 mL AsPC-1 cells suspension (5×10^7 cells/mL) into the right flank of the mice and the inoculation day was set as Day 0. The tumor length and width was measured with a dial caliper and the tumor volume was calculated according to Eq. (2):

Volume = 0.5 × Length × Width × Width   (2)

When the tumor volume reached approximately 90 mm³ on Day 8, the mice were randomized into 4 groups ($n = 6$ per group) for treatment with 5% glucose solution (Ctrl), 6 mg/kg OXA, 30 mg/kg GEM and 30 mg/kg LMPt. Each formulation was injected intravenously *via* the tail vein every three days for a total of 7 doses. The mice weight and tumor volume were measured every three days until experiment ended. And then mice were sacrificed for safety evaluation including histological feature analysis, myelosuppressive toxicity evaluation and peripheral neurotoxicity evaluation. For histological feature analysis, organs were harvested for hematoxylin−eosin (HE) staining. For myelosuppressive toxicity, blood smear was prepared. Briefly, 5 μL tail vein blood was obtained upon mice sacrifice and prepared into thin blood smear immediately on a slide, air-dried, fixed with 100% methanol and stained for 10 min with 10% Giemsa stain (DM0012, Leagene, Beijing, China), according to the method described before[36,37]. Then the stained blood smear was examined immediately under a light microscope, making sure that the cellular density of the examined area was similar. For peripheral neurotoxicity, cold hyperalgesia was set as an evaluation index according to the precious study[38−40]. Briefly, tamped ice was used to render cold environment and a thermometer was used to ensure the temperature of ice surface within 0 ± 1 °C. Then mice were placed on the ice surface for 2 min, during which the times of quick paw lifts and jumps of each mouse that demonstrate cold hyperalgesia were counted by two independent investigators.

2.8. Fluorescence microscope observation

Fluorescence microscope was employed for cellular uptake observation of DiI-LMPt. Cells were seeded in 96-well glass bottom cell culture plates and incubated with DiI-LMPt. At intended time points, the DiI-LMPt containing medium was discarded and the cells were carefully washed with PBS three times, supplemented with fresh medium. Fluoresce images of the cells at different incubation time points were recorded. Mean fluorescence intensity (FI) was analyzed using ImageJ.

2.9. Fluorescent labeling of organelles

For endosome−lysosome system and mitochondria specifical labeling, live cells were treated with early endosomes, late endosomes, lysosomes, and mitochondria labeling reagents according to the commercial instructions. For ER labelling, AsPC-1 cell stably expressing green fluorescence protein (GFP) specifically in ER lumen was established. Briefly, after transfected with sfGFP-ER-5, AsPC-1 cells were treated with G418 (2 mg/mL) for selection of the successfully transfected cells. AsPC-1-ER polyclonal cells were maintained in RPMI-1640 containing G418 (1 mg/mL). After successfully expressing the GFP signals, the cells underwent subsequently treatment.

2.10. Flow cytometry assay

Flow cytometry was used for quantitative detection of the DiI-LMPt cellular internalization. Concretely, cells, seeded in 6-well plates, were treated with DiI-LMPt for intended time points. Then cells were washed three times with cold PBS, digested from the culture plate with trypsin solution, centrifugated (4 °C, 1200 × *g*, 5 min) for collection and resuspended in 500 μL cold PBS. Finally, the mean FI of cells containing DiI-LMPt was detected and analyzed using a flow cytometry (BD Biosciences, San Jose, 207 CA, USA). A total of 10,000 events were recorded for each sample.

2.11. Inductively coupled plasma mass spectrometry (ICP-MS)

ICP-MS was used for the quantification of intracellular mass of platinum element (Pt), which was set as reference to the internalized amount of LMPt or OXA. Briefly, after treated with LMPt or OXA, the cells were washed with PBS, digested and centrifuged at $1000 \times g$ for 5 min to obtain cell pellets. Then cells were resuspended in 500 μL PBS for accurate cell counting and underwent the same centrifugation process for collection. Then 100 μL of 65% HNO_3 was added to nitrate the cells overnight followed by ICP-MS detection (ELAN DRC-II, PerkinElmer, USA). The mass of Pt in 1×10^4 cells was set as relative mass of Pt.

2.12. Endocytosis mechanism studies with endocytosis inhibitors

In the endocytosis study, cells were pre-treated with each of the endocytosis inhibitors at 37 °C for 2 h, followed by the incubation with 12 μmol/L LMPt or 12 μmol/L DiI-LMPt (the dosing based on MPt) for predetermined time points. Then LMPt uptake changes between inhibitor treated and untreated groups were compared employing fluorescence microscope investigation, flow cytometry and ICP-MS assay.

2.13. Ultra-high pressure liquid chromatography tandem mass spectrometry (UHPLC−MS/MS)

UHPLC−MS/MS was used to analyze MPt in various organelles. Briefly, after treated with LMPt, mitochondrial and ER lysates were first obtained according to the instruction of mitochondrial isolation kit (89874, ThermoFisher, MA, USA) and Endoplasmic Reticulum Isolation Kit (ER0100, Sigma−Aldrich). Then MPt, mitochondrial and ER lysates were further processed based on a liquid−liquid extraction method. Briefly, 0.2 g of homogenized sample was weighed into a 1.5 mL polypropylene tube and dissolved. The tube was shaken for 5 min and centrifuged at 15,000 rpm (3-30 KS, Sigma, Hamburg, Germany) for 5 min at 4 °C. An aliquot of the upper phase was analyzed by UHPLC−MS/MS detection. The liquid chromatography separations were performed with an Agilent 1290 Series UHPLC (Agilent, CA, USA) equipped with a quaternary pump, an auto-injector, a column heater, and a 2.7 μm pro-shell 120 EC C_8 column (2.1 mm × 50 mm, Agilent, CA, USA). Isocratic elution was performed with mobile phase consisted of methanol containing 0.1% formic acid. The total run time was 7.5 min, the flow rate was 0.3 mL/min, and the injection volume was 5 μL. The column temperature was maintained at 30 °C. The mass spectrometry was performed on an Agilent 6495 Triple Quad mass spectrometer (Agilent, CA, USA) with a positive ion mode. The optimized conditions were as follows: capillary voltage of 3500 V, nozzle voltage of 0 V, fragmentor of 380 V, and octopole RF of 750 V. The drying gas was 180 °C at 15 L/min, nebulizer gas pressure was 40 psi, and the sheath gas was 260 °C at 12 L/min. Multiple-reaction monitoring mode (MRM) was performed.

2.14. Transmission electron microscopy (TEM)

Cells were prefixed in Karnovsky's solution (1% paraformaldehyde, 2.5% glutaraldehyde, 2 mmol/L calcium chloride, 0.1 mol/L cacodylate buffer, pH 7.4) and washed with cacodylate buffer. Post-fixing was carried out in 1% osmium tetroxide and 1.5% potassium ferrocyanide for 1 h. After dehydration with increasing concentrations of ethanol (50%, 60%, 70%, 80%, 90%, and 100%), the cells were stained with 2% uranyl acetate in 70% ethanol overnight at room temperature and then embedded in Epon. The embedded samples were sectioned into 60-nm-thick slices using a sliding ultramicrotome. Thin sections supported by copper grids were examined using a JEM-1400 Plus transmission electron microscopy system (JEOL, Japan) at 120 kV.

2.15. Transfection of plasmids and siRNA

Briefly, 25×10^4 cells were cultured in 6-well plates until adherence. For plasmids transfection, 1.5 or 2.5 μL plasmids (1 μg/μL) was mixed with Lipofectamine 2000 transfection reagent (Invitrogen, MA, USA) according to the manufacturer's protocol and incubated for 5 min. The mixtures were then added to the wells of six-well plates and incubated for 6 h at 37 °C. For siRNA transfection, 50−100 nmol/L siRNA was mixed with Lipofectamine RNAiMAX transfection reagent (Invitrogen, MA, USA) according to the manufacturer's protocol and incubated for 15 min. The mixtures were then added to the wells of six-well plates and incubated for 24 h at 37 °C.

2.16. Immunoprecipitation and Western blot analysis

Cells were washed with PBS, and protein was extracted in co-immunoprecipitation buffer or RIPA lysis buffer supplemented with 1 × phenylmethanesulfonyl fluoride, followed with centrifugation (4 °C, 12,000 × g, 20 min). Total protein concentration in the supernatant was determined with Bicinchoninic Acid assay (BCA Protein Assay Kit, Beyotime, China). For immunoprecipitation, total cell lysates were immunoprecipitated with appropriate antibodies overnight at 4 °C and then incubated with Protein A/G Plus Agarose (sc-2003, Santa Cruz) for 2 h at 4 °C. After three washes at 4 °C, the immunocomplexes were mixed with 2 × sodium dodecyl sulfate (SDS) loading buffer and boiled for 10 min. For Western blot analysis, the cell lysates were mixed with 5 × SDS loading buffer and boiled for 10 min. For mitochondria protein analysis, mitochondrial extraction was first obtained according to the instruction of mitochondrial isolation kit (89874, Thermo Fisher, MA, USA) followed with the above protein extraction. Equal amounts of lysates were electrophoresed by SDS-PAGE and transferred to polyvinylidene fluoride membranes. The membranes were blocked with 5% skimmed milk at room temperature for 2 h and then immunoblotted overnight with primary antibodies at 4 °C, followed with another 2 h incubation with an appropriate secondary antibody. The immunoreactive signals were revealed using the enhanced chemiluminescence method (Millipore, MA, USA) and visualized with a Protein Simple FluorChem HD2 imaging system (ProteinSimple, CA, USA).

2.17. Immunofluorescence

Cells were washed with PBS and fixed with 4% paraformaldehyde for 30 min at 4 °C in avoid of quenching of green fluorescent protein[41]. Then the fixed cells were rinsed with PBS and permeabilized with 0.2% Triton-X-100 for 5 min on ice. After which, cells were blocked with 5% bull serum albumin for 1 h. In a humidified chamber, primary antibodies (1:200, against human albumin) were added in blocking solution and the cells were

incubated overnight at 4 °C. After rinsed with PBS, the cells were incubated with secondary antibody (1:300, conjugated to Alexa Fluor 488 to display green fluorescence signal and Alexa Fluor 633 to display red fluorescence signal) at room temperature for 40 min. Cells were then rinsed, mounted with DAPI containing mountant (P36931, Invitrogen, MA, USA) and sealed until visualization with fluorescence microscope.

2.18. RNA sequencing (RNA-seq)

Control and 30 µmol/L LMPt treated cells were sent to the Beijing Genomics Institute (BGI, Shenzhen, China) for RNA extraction, complementary DNA (cDNA) library construction and sequencing. Quality control of the raw reads enabled the downstream analysis to be based on clean reads with high quality. Sequencing was performed on a BGISEQ-500RS platform. The raw sequencing data are available in the Sequence Read Archive database in connection with BioProject F19FTSNCWLJ7274. The clean reads were mapped to the reference genome using HISAT2 (v2.0.4). Bowtie (v2.2.5) was applied to align the clean reads to the reference coding gene set, and the gene expression levels were calculated with RSEM (v1.2.12). A heatmap was drawn with heatmap (v1.0.8) according to the gene expression in different samples. Differential expression analysis was performed using the PossionDis function with thresholds of a false discovery rate (FDR) ≤ 0.001 and a $|\log2\ \text{Ritio}| \geq 1$. To gain insight into changes in phenotype, Gene Ontology (Go; https://www.geneontology.org) and Kyoto Encyclopedia of Genes and Genomes (KEGG; https://www.kegg.jp) enrichment analyses of annotated differentially expressed genes (DEGs) were performed with Phyper based on a hypergeometric test. The significance levels for terms and pathways were corrected by Q values with a rigorous threshold (Q value ≤ 0.05) *via* the Bonferroni method.

2.19. Real-time quantitative PCR (qRT-PCR) assay

Total RNA was isolated with TRIzol reagent (15596026, Invitrogen, MA, USA), while cDNA was generated using a Transcriptor First Strand cDNA Synthesis Kit (04897030001, Roche, Basel, Switzerland). The relative expression levels of specific genes were determined with an ABI 7500 Fast Real-Time PCR system (Thermo Fisher, MA, USA) employing TB Green qRT-PCR master mix (RR42LR, Takara, Beijing, China). The results were analyzed using the comparative $\Delta\Delta$Ct method.

2.20. Detection of mtDNA copy number

Total DNA was isolated from whole-cell extracts using EasyPure Genomic DNA Kit (EE101-01, TransGen Biotech, Beijing, China) according to the manufacturer's instructions. qRT-PCR was performed as previously reported[42]. Two primers were used for amplification of the gene for *ND2* in mtDNA and the β-actin gene in nuclear DNA. After the performance of qRT-PCR assay, mtDNA/β-actin ratio was calculated for each sample as an index of the relative content of mtDNA.

2.21. 8-Hydroxydeoxyguanosine (8-OHdG) detection

8-OHdG was detected as a marker of DNA damage using 8-OHdG ELISA kit (ab201734, Abcam, MA, USA). After treatment with 30 µmol/L LMPt for 24 h, cells and the corresponding medium were collected. For cell samples, total DNA was isolated and

purified as described above. The purified DNA was digested using nuclease P1 (M0660S, Biolabs, Hitchin, England), adjusted to pH 8 using 1 mol/L Tris-HCL, incubated with alkaline phosphatase at 37 °C for 30 min, boiled for 10 min and placed on ice until use. The medium samples were detected without further treatment. Then 50 µL sample and 50 µL diluted 8-OHdG antibody were added to the enzyme-labeled coating plate before sealing and incubation at 37 °C for 1 h. According to the manufacturer's instructions, the ultimate OD at 450 nm was determined.

2.22. Statistical analysis

Statistical results were presented as the mean $\pm$ standard deviation (SD) of at least three independent experiments. Statistical significance was performed using Graphpad Prism software 7.0 version (GraphPad Software company, San Diego, CA, USA). Multiple-group comparison was performed using ordinary one-way ANOVA with Dunnett's multiple comparison tests. Two-group comparison was performed using two-tailed Student's t test. $P < 0.05$ was regarded as statistical significance, symbolized by $*P < 0.05$, $**P < 0.01$, $***P < 0.001$ and not significant (ns).

3. Results

3.1. LMPt exhibits potent anti-pancreatic cancer activity in both GEM-R and GEM-S cells

Although GEM is the standard first-line drug for pancreatic cancer treatment, many patients exhibit primary or secondary resistance to it, which limits pancreatic cancer treatment. As reported in the literature[43−45], many cell lines such as MIA-PaCa-2, PANC-1, and SU.86.86 are resistant to GEM; and the cell lines such as AsPC-1 and BxPC-3 are sensitive to GEM. In this study, we used GEM-S (AsPC-1 and BxPC-3) and GEM-R (MIA-PaCa-2, PANC-1 and SU.86.86) pancreatic cancer cells to determine the anti-cancer activity of LMPt and to further evaluate the ability to overcome GEM-resistance, in which, GEM, MPt, and OXA were used as controls.

Results showed that after LMPt treatment for 24 h, both in GEM-R or GEM-S cells, cell proliferation was suppressed and the inhibition occurred in a dose-dependent manner. For example, AsPC-1 cell survival was 70.67% of the control at 0.1 µmol/L of LMPt and decreased to 28.68% at 1.6 µmol/L. When the concentration increased to 25 µmol/L, the survival was only 17.94% compared to the control (Fig. 1A), indicating that LMPt could exert a strong tumor inhibitory activity. Similar effect was observed in 48 h-treated cells. Compared with OXA and GEM, the inhibitory action of LMPt was higher at each tested concentration in both the GEM-R and GEM-S cells, indicating a superior anti-tumor efficacy of LMPt. The IC$_{50}$ of GEM, OXA and LMPt is displayed in Fig. 1B.

Then we detected MPt's anti-pancreatic effect with all the above-mentioned cells at the dose of maximal solubility of MPt in cell culture medium (1.3 µmol/L), and compared the anti-cancer effect of MPt and LMPt under this concentration. As shown in Fig. 1C, in the five pancreatic cancer cells, MPt induced poor anti-cancer activity (about 15% in 3 cells and 3% in the other 2 cells) for 48 h treatment. While at the same concentration and treated time, the inhibitory effect of LMPt was about 2.70−16.74 folds higher than that of MPt.

It was worth mentioning that, in the 24 h LMPt-treated group, a more distinct and potent anti-proliferation effect was observed compared with that of GEM and OXA. That is, the IC_{50} values of GEM in all GEM-R/S cells at 24 h were all beyond 75 μmol/L, and in OXA treated cells, the IC_{50} values also exceeded 75 μmol/L, except in MIA-PaCa-2 cells (which was still 18.52 times larger than that of LMPt). In LMPt treated cells, the IC_{50} values were between 0.28 ± 0.06 to 19.81 ± 3.57 μmol/L, indicating that 24 h treatment with GEM or OXA did not exert obvious anti-cancer activity, while there was a strong effect observed in the LMPt treated groups. When the treatment continued for 48 h, OXA and GEM began to exhibit action, but the action of LMPt was still greater than that of GEM or OXA, and the gap in action difference at 48 h was lower than that at 24 h between LMPt and GEM or OXA. The above anti-cancer assays not only demonstrated that LMPt maintained aggressive anti-pancreatic cancer ability over GEM and OXA in both GEM-S and GEM-R cell lines, but also suggested that LMPt was an anti-tumor agent characterized by rapid efficacy, indicating it is a multifunctional and promising chemotherapeutic.

Given that colony formation assay is the gold standard for the analysis of cytotoxicity[35,46], it was conducted for further comparison of the inhibitory effects between LMPt and OXA. AsPC-1 and MIA-PaCa-2 cells were seeded in 6-well plate and treated with 4, 12 or 30 μmol/L LMPt or OXA before colony counting. Results showed that, colony formation rate of LMPt-treated cells was significantly lower than that of OXA-treated cells at all treatment concentrations, indicating a superior anti-pancreatic cancer activity of LMPt compared to OXA (Fig. 1D and Supporting Information Fig. S2A). In addition, LMPt inhibited cellular colony formation in a dose-dependent manner.

Cell-number dependent inhibitory assay was also performed with SRB. $5 \times 10^4 - 50 \times 10^4$ AsPC-1 and MIA-PaCa-2 cells were seeded in 6-well plates and treated with 30 μmol/L LMPt or OXA for 24 h before SRB staining. As shown in Fig. 1E and Fig. S2B, for both AsPC-1 and MIA-PaCa-2 cells, at any cell number group treated with LMPt, almost no surviving cells were observed, compared with 10.71%−29.06% (AsPC-1) and 21.42%−58.30% (MIA-PaCa-2) cell viability in OXA-treated groups. This indicated the superior anti-cancer activity of LMPt for large numbers of tumor cells.

EdU, a thymidine analogue, can incorporate into replicating DNA during cell proliferation to reflect DNA replication[47]. Thus, the EdU assay can be used to evaluate DNA replication reflecting cell proliferation ability. The results revealed that, LMPt significantly inhibited EdU incorporation compared to OXA, indicating a stronger inhibitory effect of LMPt on DNA replication (Fig. 1F and Fig. S2C).

Besides OXA and GEM, MPt was also taking as control in colony formation assay (Fig. S2D), cell-number dependent inhibitory assay (Fig. S2E) and EdU assay (Fig. S2F) against AsPC-1 and MIA-PaCa-2 cells at the maximal solubility of MPt in medium. The results also indicated that at the same dose, LMPt exhibited more significant anti-pancreatic cancer action than MPt.

To fully understand the anti-tumor activity of LMPt, *in vivo* anti-tumor effect and the subsequent toxicity was assessed on AsPC-1 xenograft tumors in nude mice, in which OXA and GEM were used as controls. Results showed that LMPt significantly retarded tumor growth with higher tumor inhibitory action than that of GEM and OXA (Fig. 1G), as well as smaller tumor weight at the experiment endpoint (Fig. 1H). Moreover, no significant difference in body weight was observed between the LMPt treated group and the Ctrl group, however, the body weight decreased in GEM and OXA administrated groups by 21.03% and 33.07%, respectively, at the end of the treatment (Fig. 1I). This suggested less systematic toxicity and the increased *in vivo* safety of LMPt. Correspondingly, nude mice bearing GEM-R MIA-PaCa-2 xenograft tumors were also used to evaluate LMPt's effect, and similar anti-tumor activity was observed (Supporting Information Fig. S3A and S3B).

Given that LMPt is a platinum anti-cancer agent, besides general toxicity evaluation with HE staining[48,49], the platinum agent-associated toxicities such as myelosuppressive toxicity and peripheral neurotoxicity[50,51], were also examined for identifying LMPt safety. HE staining showed that in LMPt-treated mice, there was no obvious pathological damage observed in liver, spleen, kidney, intestine, or bone compared to the Ctrl group (Fig. 1J). While in the OXA treated group, we visualized obvious organ damaged, such as disappearance of white and red pulp in the spleen, damage to the glomerulus and proximal renal tubules in the kidney, and structural changes in goblet cells in the intestine. Besides, bone marrow cells decreased in the OXA treated group, indicating myelosuppressive toxicity.

In further myelosuppressive toxicity evaluation, blood smear results are shown in Fig. 1K, showing no significant difference in white blood cells in the LMPt treated group. While both numbers of white blood cells and red blood cells significantly decreased in the OXA group, which is a typical symptom of myelosuppression. For peripheral neurotoxicity, paw lifts, indicating cold hyperalgesia[50,51] are shown in Fig. 1L. No significant difference in paw lifts was observed between the LMPt and Ctrl group, while paw lifts were significantly increased in OXA treated mice. This indicates the induction of peripheral neurotoxicity by OXA.

MPt is poorly soluble in water and organic solvents[18,52] and only dissolves in 4-methylpyridine (50 °C water bath, 25 mg/mL) and DMSO (2 mg/mL, inactive in DMSO[53]). Although MPt can be dissolved in 4-methylpyridine at 50 °C, 4-methylpyridine is not suitable for *in vivo* administration, especially for intravenous injection, due to its high toxicity. Thus, MPt was not chosen as the control of *in vivo* anticancer assay at the same concentration as that of LMPt.

To elucidate the stronger *in vivo* anti-cancer effect of LMPt than MPt, we injected intravenously LMPt or MPt at the same dose (maximum solubility of MPt in 5% glucose, approximately 1 μg/mL) at the maximal injection volume of 0.5 mL (25 μg/kg) into pancreatic tumor-bearing mice every day for a total seven doses. Tumor growth and MPt content in the tumor tissue were measured. As shown in Fig. S3C and S3D, LMPt exhibited about 31.36% inhibitory effect, which was much weaker in free MPt group, approximately 4.45%. The *in vivo* inhibitory action of LMPt was about 8-fold of that of MPt. Similarly, the MPt content in tumor tissue in LMPt group was about 3-fold of that in MPt group (Fig. S3E). These results indicate that liposomal MPt increased anti-cancer action and tumor accumulation of MPt compared with that of free MPt.

3.2. Faster cellular uptake-induced large accumulation contributes to the potent anti-tumor efficacy of LMPt

We next explored the anti-cancer mechanism of LMPt. As a liposomal formulation, LMPt should be characterized by superior advantage in drug load and intracellular drug delivery. As reported previously, the Pt in platinum agents including MPt, is the main effector responsible for inducing anti-cancer efficacy[54−59]. Thus,
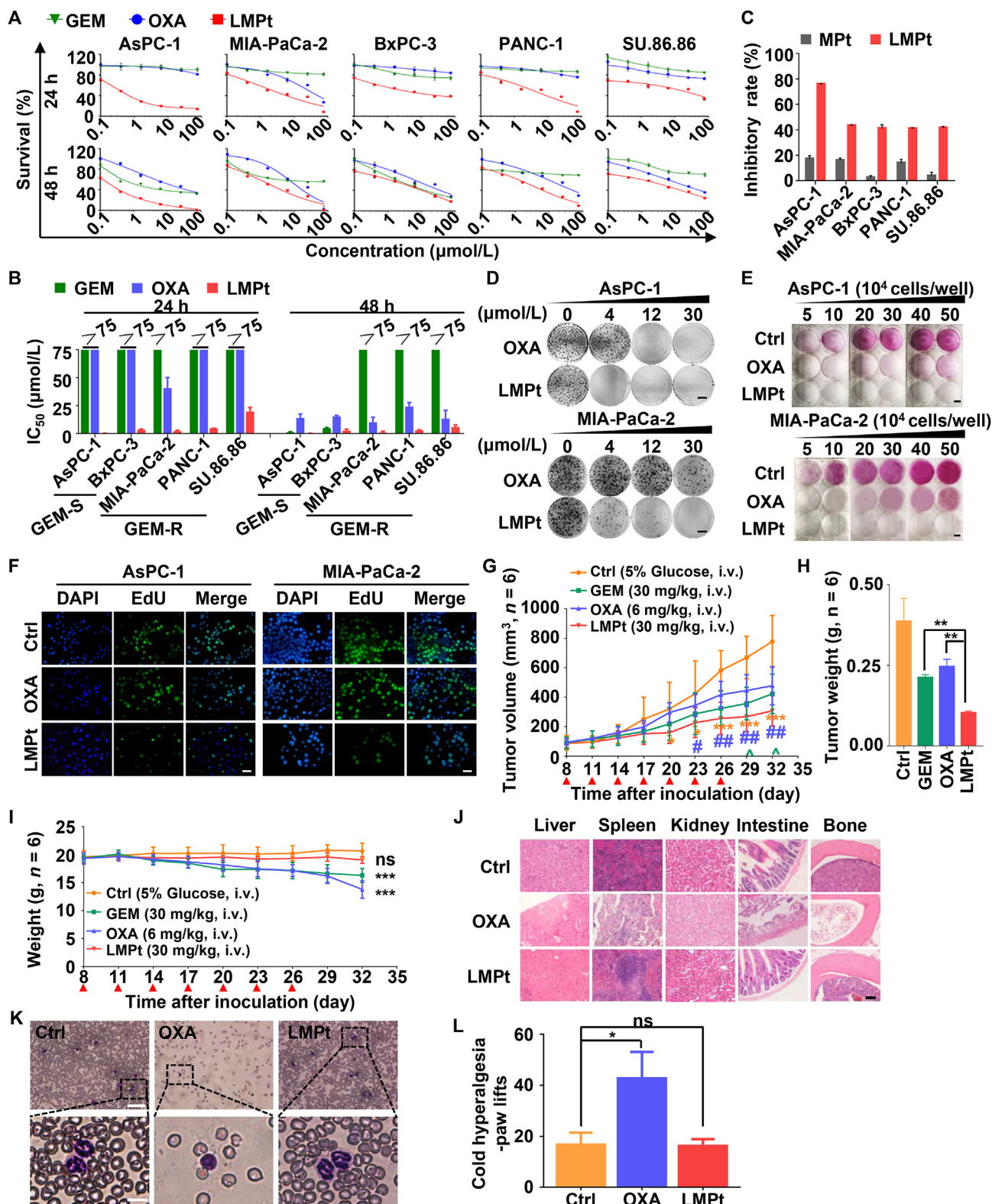
Figure 1 LMPt exhibits potent anti-pancreatic cancer activity in both GEM-S and GEM-R cells. (A) GEM-S cells AsPC-1 and BxPC-3, and GEM-R cells MIA-PaCa-2, PANC-1 and SU.86.86 were treated with the indicated concentrations of GEM, OXA or LMPt for 24 or 48 h, and cell survival was detected with MTT assay. Survival (%) = $(OD_{tested}-OD_{blank})/(OD_{Ctrl}-OD_{blank}) \times 100$. A dose-dependent survival curve was plotted using SigmaPlot software. (B) IC_{50} of GEM, OXA and LMPt in different pancreatic cancer cells (GEM-R/S), calculated using SigmaPlot 10.0 by standard curve analysis. (C) The indicated pancreatic cancer cells were treated with MPt or LMPt at the maximal solubility of MPt in medium for 48 h, and cell vitality was detected with MTT. Inhibitory rate (%) = $[1-(OD_{tested}-OD_{blank})/(OD_{Ctrl}-OD_{blank})] \times 100$. (D) GEM-S cells AsPC-1 or GEM-R cells MIA-PaCa-2 were seeded in 6-well plate at 1000 cells/well. After 24 h, 4−30 μmol/L LMPt or OXA was added and continued to

we hypothesized that the higher Pt accumulation in cells may mediate LMPt's superior anti-cancer activity. Correspondingly, we detected the amount of intracellular Pt, to evaluate whether liposome dosage contributed to Pt internalization, using MPt's structural analog, OXA, as control. Time-dependent accumulation results (Fig. 2A left) showed that in LMPt-treated cells, the Pt amount sharply increased in response to LMPt addition. After 1 h incubation, the amount of Pt in LMPt treated cells was about 2.60 times higher than that of the OXA-treated cells, and after 24 h the amount of Pt increased to 5.26 times higher than that of OXA. The increased rate was sustained for 48 h after LMPt addition. In OXA treated cells, we only observed a minor elevation in the Pt amount within the first 12 h and then until 48 h the Pt amount was in a platform period (Fig. 2A left). The total accumulation amount of Pt in the LMPt group was 8.91 times larger than that of the OXA group until the experiment endpoint at 48 h, indicating a rapid accumulation of Pt after addition of LMPt. LMPt accumulation also increased in a dosage-dependent manner (Fig. 2A middle) and the Pt amount was larger than that in OXA treated cells at any dosage of LMPt, which might elucidate why LMPt exhibits a more potent anti-cancer action. While at the dose of maximal solubility of MPt in cell culture medium, MPt-induced Pt accumulation is very low (about 0.1 ng/10^4 cells) at 6 h and with elapse of time the accumulated amounts of Pt only increased slightly (Fig. 2A right), which was in accordance with its poor anti-cancer activity (Fig. 1C). However, at the same concentration (maximal solubility of MPt in cell culture medium), LMPt induced significantly Pt accumulation at 6 h and accumulated amounts of Pt was 1.64-fold of that of MPt. With time elapsed, LMPt-induced Pt accumulation gradually increased and up to 48 h the accumulated amounts of Pt were 7.06-fold of that of MPt (Fig. 2A right). These results indicate that LMPt accumulated largely, and the accumulation rate was much higher than that of MPt and OXA.

Usually, cellular accumulation of nanoparticles is a balanced result of both exocytosis and endocytosis[60−62], so is LMPt. Based on this, firstly we examined the exocytosis proteins related to Pt (ATP7A, ATP7B, GSTP1 and MRP2)[25,63−66] under the same conditions where Pt accumulation was observed, and found LMPt treatment did not change these exocytosis proteins level significantly (Supporting Information Fig. S4A), indicating that exocytosis of Pt might not involve in LMPt accumulation, and cellular uptake of LMPt was the dominant contributor to Pt accumulation. Conclusively, just the faster and sustained uptake-induced larger accumulation of LMPt than that of OXA contributed to the potent anti-pancreatic action of LMPt over OXA.

Then, we further explored uptake dynamics of LMPt to clarify the potential reason of faster entry into cells of LMPt. LMPt was labeled with fluorescence DiI (DiI-LMPt) and its cellular uptake dynamics were observed. Results (Fig. 2B and Fig. S4B) show that after 10 min of DiI-LMPt addition, there was obvious accumulation of DiI-LMPt in AsPC-1 cells, but no obvious cellular accumulation of DiI-LMPt was visualized in MIA-PaCa-2 or BxPC-3 cells until 30 min post cellular exposure. These results indicate that in various cells, the speed of cellular uptake of LMPt (evaluated by starting uptake time of Dil-LMPt) was different, although hereafter the amount of DiI-LMPt all increased in a time-dependent style.

Given that the rapid uptake-induced large accumulation is crucial to LMPt action and the cellular uptake rate of LMPt is different in various cells, we questioned whether the uptake rate of LMPt was the mediator of its anti-cancer action. That is, quicker cellular uptake, stronger anti-cancer activity of LMPt? Therefore, we assessed the correlation between the starting time of obvious cellular uptake of LMPt and the IC_{50} using time-lapse photography (Supporting Information Fig. S5) in 5 cell lines. Results show in AsPC-1 cells, the starting time of obvious cellular uptake was the shortest, and its IC_{50} was also the lowest among all 5 tested cell lines. The starting uptake time was similar in MIA-PaCa-2, BxPC-3 and PANC-1 cells, as were their IC_{50} values. Moreover, SU.86.86 cells had the largest IC_{50} and its cellular uptake was also the slowest.

Next, we quantitatively detected the amount of LMPt cellular entry by flow cytometry to further evaluate the correlation between IC_{50} and the cellular entry dynamics of LMPt. Mean FI, indicating accumulating amount of LMPt at various time points was plotted (Fig. 2C), which supported the previous results that the LMPt uptake amount was the highest in AsPC-1 cells, similar in MIA-PaCa-2, BxPC-3, and PANC-1 cells and lowest in SU.86.86 cells. These results indicate that the uptake time was delayed from AsPC-1 to SU.86.86 cells, corresponding to their increased IC_{50} values. Finally, linear regression was analyzed among the five cell lines, verifying that the starting cellular uptake time was positively correlated with the corresponding IC_{50} values (Fig. 2D). Correspondingly, the earlier starting time of LMPt uptake should lead to larger final accumulating amount. And the total amount of LMPt at 24 h was also proved to decrease from AsPC-1 to SU.86.86 cells (Fig. 2C), which was negatively correlated with the anti-cancer action (Fig. 2E). These results show that faster cellular entry mediated increased accumulation was the key of the potent action of LMPt. Additionally, the rate difference of LMPt cellular entry in various cells decided the sensitivity of pancreatic cancer cells to LMPt. Notably, in Pt accumulation and the following other intracellular fluorescence assays, we utilized higher concentrations of LMPt (12 or 30 μmol/L) compared with its IC_{50} value, and at this higher concentration it seems no cell alive based on IC_{50} curve. That is, IC_{50} value was acquired based on 96-well culture plate. But in Pt accumulation and the following many assays, 6-well plate was utilized since more cells were needed. In fact, under the same dose the inhibitory effect of LMPt

---

incubate for 10 days. Then visible colonies were photographed. Scale bar, 8 mm. (E) $5 \times 10^4 − 50 \times 10^4$ AsPC-1 or MIA-PaCa-2 cells were seeded in a 6-well plate. After 24 h, 30 μmol/L LMPt or OXA was added and incubated for 48 h continuously, cellular survival was evaluated by SRB assay. Scale bar, 8 mm. (F) AsPC-1 or MIA-PaCa-2 cells were treated with 30 μmol/L LMPt or OXA for 24 h, and cell proliferation was detected with EdU assay. Scale bar, 40 μm. Nude mice bearing AsPC-1 cells were administered 30 mg/kg GEM, 6 mg/kg OXA or 30 mg/kg LMPt when tumor volume reached 100 mm^3 (every three days, total 7 administrations, $n = 6$). When the experiment ended, mice were sacrificed and tumors and various tissues were excised. The curve of tumor volume (mm^3) (G), final tumor weight (H) and body weight (I) were monitored and plotted. In the curve of tumor volume, *$P < 0.05$, ***$P < 0.001$, LMPt *vs.* Ctrl; #$P < 0.05$, ##$P < 0.01$, LMPt *vs.* OXA; ^$P < 0.05$, LMPt *vs.* GEM. Red arrows stood for administration time. The representative images of HE staining of various tissues, scale bar, 100 μm (J) and blood smear stained with Giemsa, scale bar, 100 μm (upper panel) and 20 μm (bottom panel) (K) are shown. Cold hyperalgesia (taking raw lift counts as index) was conducted for peripheral neurotoxicity evaluation (L). ns, no significant; *$P < 0.05$; **$P < 0.01$, ***$P < 0.001$, compared with Ctrl or 0 μmol/L treated group, unless specifically indicated. All the data are shown as mean $\pm$ SD ($n = 3$).
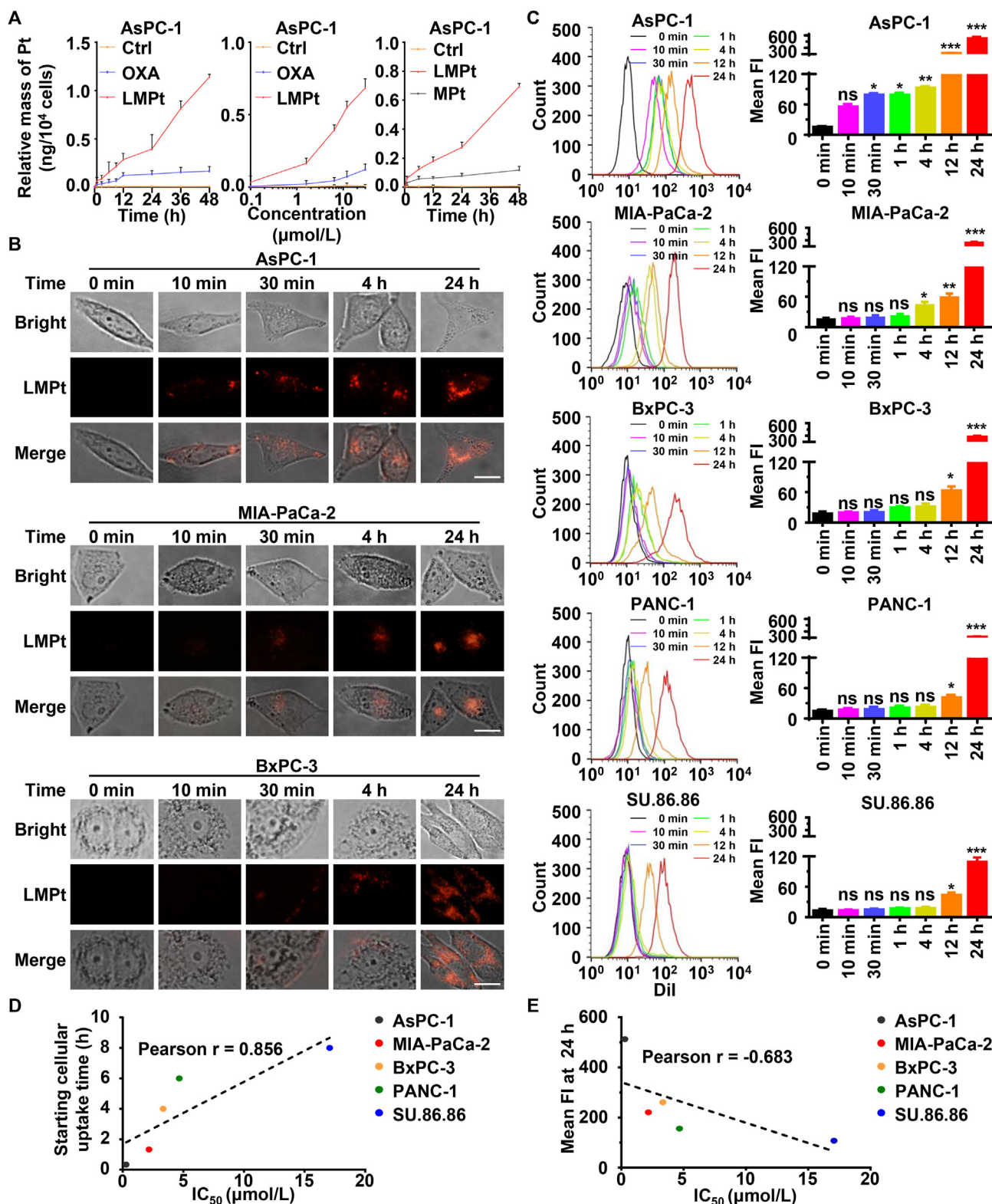
Figure 2 LMPt induces fast and abundant Pt accumulation which is positively correlated with antitumor action in cells. (A) AsPC-1 cells were treated with 12 μmol/L LMPt or OXA for indicated time (left), or were treated with indicated doses of LMPt or OXA for 24 h (middle), or were treated with LMPt or MPt at the maximal solubility of MPt in cell culture medium (right), then cells were lysed for Pt measurement with ICP-MS and time and dose-dependent curves of Pt accumulation were plotted. The indicated cells were treated with DiI-labeled LMPt and intracellular accumulation of LMPt was detected with fluorescent microscope (B), and flow cytometry (C). Correlation of IC_{50} with starting cellular uptake time of LMPt (D) and uptake amount (mean FI) at final time points (E) were analyzed. Scale bar, 20 μm. ns, no significant; $*P < 0.05$, $**P < 0.01$, $***P < 0.001$, compared with mean FI at 0 min. All the data are shown as mean $\pm$ SD ($n = 3$).

in 96-well plate and 6-well plate is different. Taking AsPC-1 as an example, at 12 μmol/L of LMPt for 24 h treatment, in 96-well plate, the cell survival was about 17.67%, while in 6-well plate is 55.74%, and 42.89% at 30 μmol/L. That is a result of different acquired compound amounts of each cell in 96-well and 6-well plate, based on the diverse numbers of seeded cell and volume of added medium according to manufacturer's guidance and assay procedure.

3.3. Caveolae-mediated endocytosis and macropinocytosis involve in endocytosis of LMPt

Since fast cellular entry mediated large accumulation is the key for LMPt anti-cancer action, and different cellular uptake rate of LMPt resulted in different anti-cancer action in various cells, we further explored why LMPt could be taken up quickly and why the uptake rate were diverse in various cells. LMPt is a liposome with particle size around 100 nm[29]. Previous reports have shown that liposomes around 100 nm have three possible pathways to mediate cellular entry: clathrin-mediated endocytosis (CME), caveolae-mediated endocytosis, and macropinocytosis[67–69]. Accordingly, various inhibitors against these three pathways (Supporting Information Table S1) were introduced to determine which pathway would diminish cellular entry of LMPt and thus to verify the pathway mediating LMPt entry.

For CME, CPZ, a cationic amphiphilic drug, and siClathrin were used for specific blockage of CME by disrupting clathrin on the cell surface[70]. For caveolae-mediated endocytosis, due to Cav-1 and cholesterol are all important players in caveolae formation, genistein (which blocks phosphorylation of Cav-1 and is required for caveolae formation)[71] and nystatin (a cholesterol sequestering agent, which triggers the absence of lipid rafts and caveolae)[72–74] were both used to evaluate the LMPt entry pathway by inhibiting caveolae-mediated endocytosis. For macropinocytosis, actin polymerization-based membrane ruffles (protrusion) which subsequently forms vesicles to carry the outer particles enter cell was prerequisite. CytoD (inhibiting actin polymerization) and amiloride (inhibiting cellular membrane ruffling *via* blocking Na^+/H^+ ion channel) were used as macropinocytosis inhibitors[75]. Before the endocytosis inhibiting test, we evaluated the cytotoxicity of the above inhibitors on AsPC-1, MIA-PaCa-2 and BxPC-3 cells at the concentrations causing minimal damage (the decreased survival is lower than 25%) for the subsequent study (Table S1 and Supporting Information Fig. S6).

After LMPt was added in the presence or absence of these inhibitors, we utilized three techniques to comprehensively compare the endocytosis blocking ability of those inhibitors in all 5 cell lines: fluorescence microscope for qualitative observation (Fig. 3A and Supporting Information Fig. S7A), flow cytometry for quantitative determination (Fig. 3B and Fig. S7B) and ICP-MS assay which finally defined accurate Pt amount (Fig. 3C and Fig. S7C). Results show that in various pancreatic cancers, the endocytosis pathways of LMPt were different. For example, in AsPC-1 cells, inhibitors of the caveolae-mediated pathway (genistein and nystatin) significantly weakened cellular accumulation of DiI-LMPt by about 67.77% (genistein) and 36.53% (nystatin) (Fig. 3A), flow cytometer (Fig. 3B) and ICP-MS (Fig. 3C) assays further verified these effects. Macropinocytosis pathway inhibitors (CytoD and amiloride) decreased LMPt endocytosis by 21.53% (CytoD) and 60.05% (amiloride) (Fig. 3A) and similar inhibitory effects were observed *via* flow cytometry and ICP-MS detection (Fig. 3B−C). While the CME inhibitor CPZ and clathrin-depleted

agent siClathrin did not interfere with LMPt endocytosis (Fig. 3A−C and Fig. S7D). Similar results mentioned above were also observed in MIA-PaCa-2 cells (Fig. S7A−S7C). These results showed in highly LMPt-sensitive AsPC-1 and MIA-PaCa-2 cells, caveolae and macropinocytosis-mediated endocytosis together mediated LMPt endocytosis.

In BxPC-3 cells, which are less sensitive to LMPt than AsPC-1 and MIA-PaCa-2 cells, only inhibitors of caveolae-mediated pathway (genistein and nystatin) exhibited obvious endocytosis inhibition effect on LMPt (69.38% for genistein and 13.22% for nystatin). Both CME inhibitor (CPZ) and macropinocytosis inhibitor (CytoD and amiloride) caused little change in LMPt endocytosis (Fig. S7A−S7C). The inhibition results in PANC-1 and SU.86.86 cells (which are also less sensitive to LMPt than AsPC-1 and MIA-PaCa-2) showed similar effects as BxPC-3 (Fig. S7A). These results demonstrated in less LMPt-sensitive cells, only the caveolae-mediated pathway mediated LMPt endocytosis, indicating that the endocytosis mechanism for LMPt varies among different pancreatic cancer cells. Additionally, we also detected MPt entry pathways and found the inhibitors of Cav-1 mediated-endocytosis (genistein and nystatin) and macropinocytosis (CytoD and amiloride) did not interfere with Pt intake of MPt (Fig. S7E), thus the cellular entry pathways are different between LMPt and MPt.

Thus, in cells characterized by faster cellular entry and stronger anti-cancer effects of LMPt, caveolae-mediated endocytosis and macropinocytosis coordinately promoted the endocytosis of LMPt. However, in cells with a slower entry rate and decreased anti-cancer effects, caveolae-mediated endocytosis, alone, mediated endocytosis of LMPt, hinting that macropinocytosis might play a more active role in the initial phase of LMPt endocytosis.

3.4. In high Cav-1 cells, Cav-1 mediates LMPt endocytosis, and in low Cav-1 cells, macropinocytosis and Cav-1 induced by LMPt contribute to LMPt endocytosis together

We explored why differential pathways are involved in LMPt entry in various cells. Since caveolae-mediated endocytosis was the common pathway for LMPt entry in all tested pancreatic cells[67], we paid close attention on the Cav-1, the main effector protein. Analysis of Cav-1 level in the five pancreatic cancer cells showed that in BxPC-3, PANC-1, and SU.86.86 cells, Cav-1 expression was higher than that of AsPC-1 and MIA-PaCa-2 cells. Meanwhile, the level of Cav-1 decreased in the order of BxPC-3, PANC-1 and SU.86.86 cells according to LMPt accumulation amount (Fig. 3D and Supporting Information Fig. S8A), indicating that in cells where caveolae mediating endocytosis, Cav-1 might be a determinant of LMPt entry. For further verification, *Cav-1* was knocked down *via* siRNA (Fig. S8B) and results show that Cav-1 silencing restricted cellular entry of LMPt (Fig. 3E), further demonstrating that Cav-1 was the major determinant of LMPt entry in cells with caveolae-mediated endocytosis as the only endocytosis pathway. Actually, Cav-2, another subtype of caveolin, proved to be ineffective for LMPt endocytosis, consistent with previous reports (data not shown)[76,77].

Then we wanted to ascertain in low-Cav-1 expressing AsPC-1 and MIA-PaCa-2 cells, how macropinocytosis and caveolae-mediated endocytosis coordinately contributed to LMPt endocytosis. In AsPC-1 and MIA-PaCa-2, although caveolae-mediated endocytosis also participated in LMPt entry, we found Cav-1 level was very low. Thus, we hypothesized that LMPt induced increased
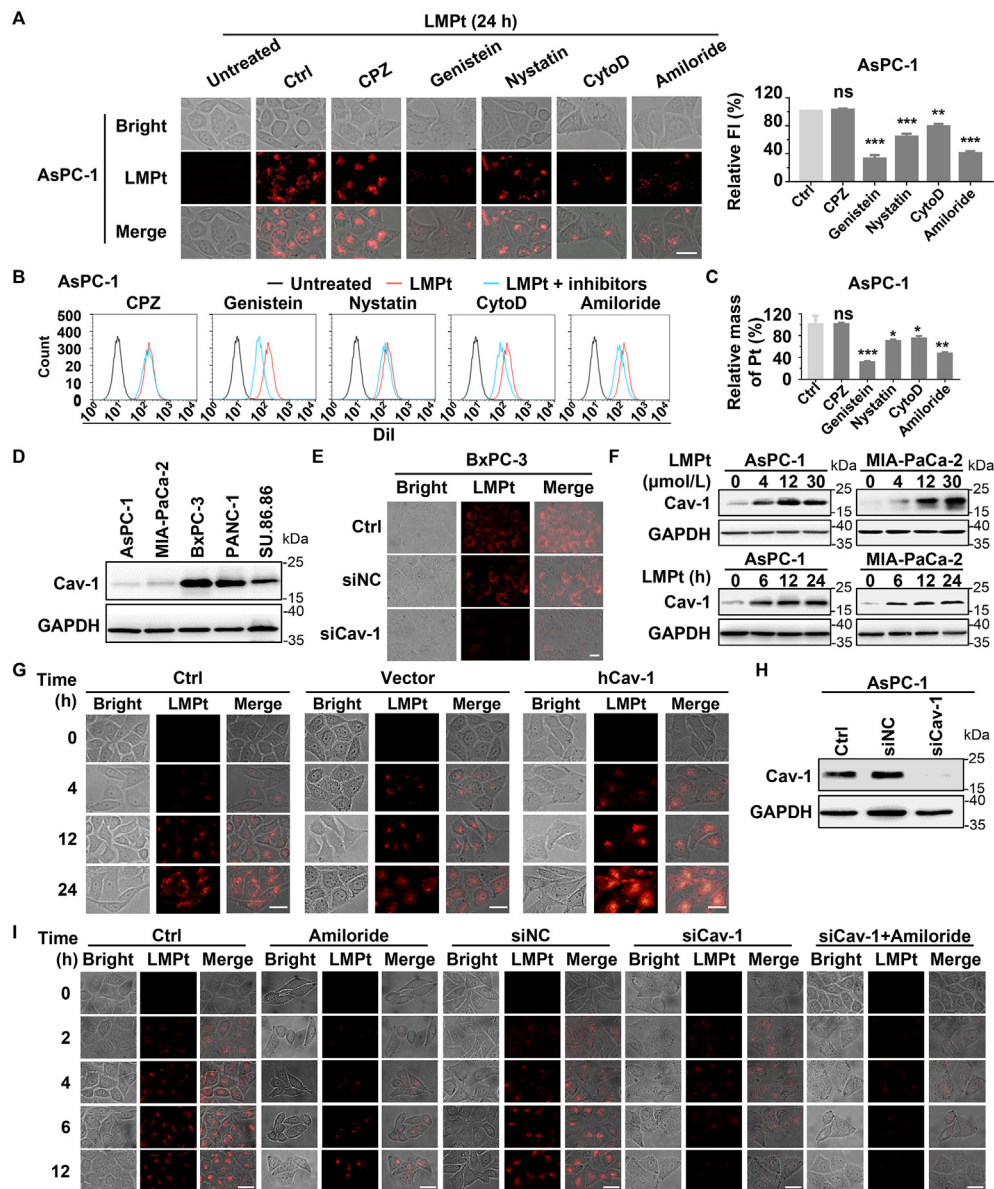
Figure 3 In high Cav-1 cells, Cav-1 mediates LMPt endocytosis, and in low Cav-1 cells, macropinocytosis and Cav-1 induced by LMPt contribute to LMPt endocytosis together. AsPC-1 cells were treated with or without indicated endocytosis inhibitors for 2 h followed by exposure to LMPt for 24 h, LMPt accumulation was observed with fluorescent microscope (A), flow cytometry (B) and ICP-MS (C). Scale bar, 20 μm. ns, no significant; *P < 0.05, **P < 0.01, ***P < 0.001, *vs*. Ctrl. The data are shown as mean ± SD (n = 3). (D) Western blot analysis of endogenous Cav-1 in different pancreatic cancer cells. (E) BxPC-3 cells were transfected with si*Cav-1* or siNC, cellular accumulation of LMPt was detected with fluorescence microscope. Scale bar, 20 μm. (F) Cells were treated with indicated concentrations of LMPt for 24 h or with 30 μmol/L LMPt for the indicated time, Cav-1 protein was detected by Western blot. (G) AsPC-1 cells were transfected with Cav-1 or vector, and LMPt accumulation was observed with fluorescence microscope, scale bar, 20 μm. (H) AsPC-1 cells were treated with LMPt and si*Cav-1*, then Cav-1 level was detected with Western blot. (I) AsPC-1 cells were treated with si*Cav-1* in the presence or absence of indicated inhibitors followed by exposure to LMPt. LMPt accumulation was observed with fluorescence microscope. Scale bar, 20 μm.

Cav-1 expression and then the increased Cav-1 mediated LMPt endocytosis. Therefore, we detected Cav-1 expression following addition of LMPt, and found Cav-1 expression indeed increased after the 6 h addition of LMPt and the increase was in a dose- (Fig. 3F upper and Fig. S8C) and time- (Fig. 3F below and Fig. S8C) dependent manner. Further, qRT-PCR results indicated that the mRNA levels of *Cav-1* also increased (Fig. S8D).

To confirm whether the LMPt-induced Cav-1 expression was involved in LMPt endocytosis, we first knocked down *Cav-1* and

observed whether decreased Cav-1 could restore LMPt entry. Results reveal that *Cav-1* knockdown could withdraw LMPt entry, indicating that the LMPt-induced Cav-1 increase was involved in LMPt cellular entry (Fig. 3H–I, the third and fourth row). Second, we overexpressed Cav-1 (Fig. S8E) and determined whether the elevated Cav-1 could enhance LMPt entry. Results show that *Cav-1* increase indeed significantly promoted LMPt endocytosis (Fig. 3G). All these results indicate that LMPt-induced Cav-1 increase may play a key role in LMPt cellular entry.
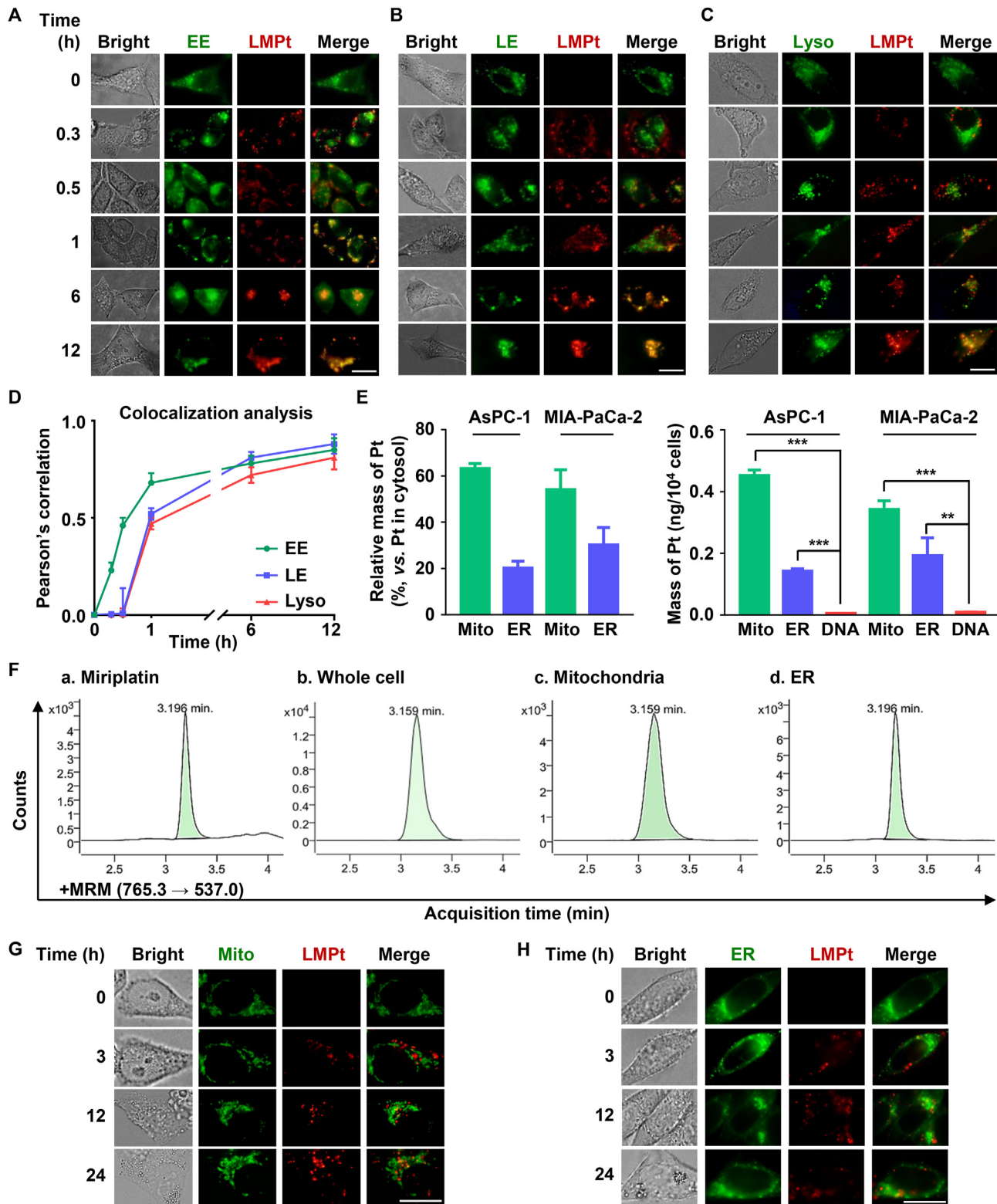
Figure 4   In unchanged metabolite, MPt targets to mitochondria and ER after LMPt is transported by endosome−lysosome. AsPC-1 cells were transfected with various GFP-labeled proteins of early endosome (EE), late endosome (LE), lysosomes (Lyso) followed by treatment with 12 μmol/L LMPt for intended times, colocalization of LMPt with EE (A), LE (B), Lyso (C) was taken with confocal fluorescence microscope. Scale bar, 20 μm. Quantitative analysis of colocalization of LMPt with EE, LE and Lyso was evaluated using Pearson's correlation coefficient based on ImageJ (D). (E) AsPC-1 and MIA-PaCa-2 cells were treated with 12 μmol/L LMPt for 24 h and Pt mass in mitochondria (Mito), ER and DNA was measured by ICP-MS. **$P < 0.01$, ***$P < 0.001$. The data are shown as mean ± SD ($n = 3$). (F) AsPC-1 cells were treated with 12 μmol/L LMPt for 24 h and mitochondria and ER fraction were extracted for MPt and its metabolites analysis by UHPLC−MS/MS. AsPC-1 cells were transfected with various GFP-tagged proteins of mitochondria (Mito) and ER followed by treatment with 12 μmol/L LMPt for intended times, colocalization of LMPt with Mito (G) and ER (H) was taken with confocal fluorescence microscope. Scale bar, 20 μm.

Given that Cav-1 need to be induced for expression, and it could be observed that the induced Cav-1 began to take effect after 6 h of LMPt addition, we speculated in the first 6 h of LMPt addition, additional endocytosis *via* macropinocytosis might mainly be in charge of LMPt cellular entry. That is, companied with Cav-1 increase, macropinocytosis and caveolae-mediated endocytosis coordinately contributed to LMPt endocytosis. As shown in Fig. 3I, we first blocked macropinocytosis (by amiloride, the second group) and found that macropinocytosis blockage inhibited LMPt entry at the first 6 h of LMPt addition. After 6 h, although its inhibition effect declined, the LMPt entry was still observed decreased compared to the Ctrl group, indicating that macropinocytosis played a role through the whole process of LMPt endocytosis.

Second, we blocked Cav-1-mediated endocytosis (by siRNA, Fig. 3I, the third and fourth groups) and observed whether LMPt entry was inhibited in the first 6 h of LMPt addition. Results showed that LMPt entry was not restricted before the first 6 h of LMPt addition, and after 6 h restricted entry of LMPt was observed, indicating that caveolae-mediated endocytosis played a dominant role after Cav-1 was induced after 6 h of LMPt addition. Finally, we simultaneously suppressed caveolae-mediated endocytosis and macropinocytosis (Fig. 3I, the last group), revealing that the LMPt entry was completely inhibited throughout the whole experiment. These data further verified that macropinocytosis and caveolae coordinately contributed to endocytosis.

Taken together, Cav-1 level was the key to LMPt endocytosis pathways. In high-Cav-1 cells, caveolae-mediated endocytosis promoted LMPt endocytosis, and Cav-1 level determined the sensitivity to LMPt. While in low-Cav-1 cells, macropinocytosis assisted the cellular entry of LMPt at the beginning of the endocytosis process. With the expression increasing of Cav-1 induced by LMPt addition, caveolae-mediated endocytosis began to take dominant role in cellular entry of LMPt.

3.5. In unchanged metabolite, MPt targets to mitochondria and ER after LMPt processing by endosome−lysosome

Generally, after nanoparticles entering cells *via* caveolae-mediated endocytosis and macropinocytosis, the nanoparticles would be fused into early endosomes, which mature to late endosomes, and further fuse with lysosomes for nanoparticle degradation. Finally, the active agents from the degraded nanoparticle would execute pharmacological activity[67,78,79]. To determine if this same process applies to LMPt cellular transportation and processing after cell entry, we utilized GFP-labeled proteins in early endosomes, late endosomes and lysosomes to observe the LMPt route in cells. These labeled proteins were fused proteins: GFP-Rab5a which localizes in early endosomes, GFP-Rab7a which localizes in late endosomes and GFP-LAMP1 (lysosome associated membrane protein 1) which localizes in lysosomes. Then we transfected these labeled proteins and added DiI-LMPt to observe whether DiI-LMPt entered these organelles and timing of entry *via* time-lapse photography.

Results showed that LMPt began to enter early endosomes after 0.5 h addition of LMPt, entered late endosomes after 1 h, and then the lysosomes according to the colocalization observation (Fig. 4A−C) and the quantitative analysis of colocalization with Pearson's correlation (Fig. 4D). These results show that LMPt, as other usual nanoparticles[80], was transported by the endosome−lysosome system after endocytosis.

Given that MPt is the core anti-cancer molecule of LMPt and Pt is the effector of MPt, we aimed to track the whereabouts of the effector, Pt, after endosome−lysosome processing. Thus, we extracted various cell organelles characterized by big size, large numbers and essential to survival (because these traits make them more likely to become target), such as nuclear DNA, mitochondria and ER, etc., and detected the mass of Pt by ICP-MS. Results turned out that only trace Pt was detected in nuclear DNA, but more than 80% Pt was found in membranous organelles: mitochondria (62.91% in AsPC-1, 53.80% in MIA-PaCa-2) and ER (19.92% in AsPC-1, 29.91% in MIA-PaCa-2) in cytoplasm (Fig. 4E left). Pt in nuclear DNA was significantly less than that in both the mitochondria and ER (AsPC-1: 129.96 times and 40.93 times less than that of the mitochondria and ER, respectively; MIA-PaCa-2: 48.29 times and 27.21 times less than that of the mitochondria and ER, respectively. Fig. 4E right), indicating the primary targeting organelle of LMPt is the mitochondria and ER.

Then the further question is coming, is the unchanged MPt or its metabolites that targeting these organelles? To solve this, we introduced UHPLC−MS/MS that could trace molecular fragments containing Pt to explore the final metabolite form of MPt. As shown in Fig. 4F, unchanged MPt was detected in the cell (Fig. 4Fb), which was in both mitochondria (Fig. 4Fc) and ER lysates (Fig. 4Fd) based on the same retention time as MPt (3.1 min) (Fig. 4Fa). Except for the unchanged MPt, we did not find other forms of Pt metabolites, indicating that after processing by the lysosome, MPt, in unchanged metabolite form, enters target organelles. The above results indicated that after LMPt degrading by lysosomes, MPt was released from LMPt, the intact molecular form of MPt targeted to mitochondria and ER.

Previous reports show that some nanoparticles could escape from the lysosome and directly target to the organelles after endosome−lysosome processing[80]. Given this fact, we continued to test whether LMPt targeted mitochondria and ER directly after entering cells. The colocalization showed that LMPt did not directly target the mitochondria and ER after entering cells (Fig. 4G−H). Together these results showed that after cellular entry, LMPt was degraded in lysosomes and then MPt was released from LMPt and targeted to mitochondria and ER in intact molecule form. Correspondingly, we also detected the cellular location of MPt and found that MPt in mitochondria and ER were all below the limit of detection of ICP-MS (0.01 ng/mL), indicating that no MPt was found in mitochondria and ER. But in DNA, a small amount of accumulated Pt was detected (data not shown), indicating the distinct targets of LMPt and MPt in cells.

3.6. Instead of DNA damage, mitochondria-induced mitophagy mediates anti-cancer action of LMPt

Next, we wanted to know what pathology was induced by LMPt to mediate the anti-cancer effects. First, we observed morphology changes under light microscopy in response to LMPt treatment. As displayed in Fig. 5A−B, after treated with LMPt either in AsPC-1 or MIA-PaCa-1 cells, many large and membrane-surrounded vacuoles were observed in the cytoplasm. Moreover, the amounts of empty vacuoles increased in a treatment dose- and time-dependent style, indicating obvious correlation between empty vacuoles and LMPt.

To further investigate the relationship between these vacuoles and the anti-cancer activity of LMPt, we introduced TEM for a more precise observation. Under TEM, we found various types of vacuoles surrounded by membranes (Fig. 5C), among them some

were large and empty, some contained incomplete organelles at various degrading stages. These changes are usually regarded as the hallmark features of autolysosomes, as previously described[81−83].

Following in-depth observation, we found considerable swollen mitochondria in cells treated for 12 h (Fig. 5CI). Furthermore, as shown in Fig. 5CII, in 24 h treated cells, broken mitochondrial degradation remnants were observed according to cristae structure (the specific structure of mitochondria) in most of autolysosomes, which were disorganized, fragmented, and distorted, indicating mitophagy. These pathological morphology changes may display a pathological process development of mitochondrial changes during treatment, from initial mild stages (swollen mitochondrial response to the potential damage or dysfunction) to the more serious stage (mitophagy).

Meanwhile, we observed the fusion process of these autophagy vacuoles: the two small empty vacuoles with similar sizes were fusing to form a bigger vacuole (Fig. 5CIII), and the large vacuoles could further engulf other small vacuoles to form even larger vacuoles, as reported before (Fig. 5CIV)[84,85], which may explain the formation of large empty vacuoles. Correspondingly, mitochondrial proteins labeled with GFP was transfected into cells to monitor morphology changes of mitochondria, showing that mitochondria changed from normal baton or filamentous to vacuoles, and these vacuoles continued to enlarge with the extension of the treatment time (0−48 h, Supporting Information Fig. S9A). These results are in accordance with the vacuoles observed under the light microscope (Fig. 5A−B) and indicate that mitophagosomes induced by LMPt treatment resulted in large empty vacuoles in the cytoplasm, which may be a reason for the final death of the cells.

Then, we detected signal pathway changes by RNA-seq microarray analysis, which gave the consistent evidences and comprehensive data of molecular pathways of cells. Three types of pancreatic cancer cells (AsPC-1, MIA-PaCa-2, and BxPC-3) were treated with LMPt and mRNA was extracted for RNA-seq analysis. DEGs in treated cells *vs.* control cells were obtained based on the transcriptomic data. 169 overlapping DEGs were found among the three comparison groups (Ctrl *vs.* LMPt for AsPC-1, MIA-PaCa-2, and BxPC-3 cells) and were analyzed (| log2 Ratio| $\geq$ 1, *FDR* $\leq$ 0.001, Fig. S9B). KEGG pathway classification analysis of these 169 DEGs shows that mitophagy-associated pathways occupied most of the DEGs (Fig. 5D). Moreover, in the three tested cells, KEGG pathway enrichment analysis also proved that mitophagy was significantly enriched among several pathways related to cell death (Fig. 5E and Fig. S9C). These results further verify mitophagy induced after LMPt treatment at the genomic level.

We also explored the molecular mechanism of weak anti-cancer activity of MPt with RNA-seq microarray analysis. Results showed that MPt only induced slight molecular pathways changes (only about 20% pathways occurred feeble changes among all pathways), and these effected pathways are focused on DNA adducts-leading effect (Fig. 5F−G).

We then analyzed the expression of vital autophagy marker LC3B (increase of LC3B level is usually interpreted as autophagy activation) by Western blot[86,87]. Results indicated that the LC3B level was obviously elevated (Fig. 5H and Fig. S9D) in the presence of LMPt and the increased LC3B were located in mitochondria, when visualized *via* colocalization analysis of mitochondria and LC3B (Fig. 5I and Fig. S9E). Further, colocalization was also proved between the mitochondria and lysosomes, which usually digest the disabled organelles in autophagic

vacuoles (Fig. 5J and Fig. S9F). These results indicate autophagy aroused in mitochondria after LMPt addition.

Then, we explored the detailed molecular mechanism of mitophagy occurrence. Generally, the PINK1-Parkin axis is considered as a canonical pathway mediating mitophagy[88]. Under physiological conditions, PINK1 is positioned between the outer mitochondrial membrane and inner mitochondrial membrane, and is cleaved by inner mitochondrial membrane-bound proteases and degraded by the proteasome, leading to undetectable basal levels of PINK1[89]. When mitochondria are defective, PINK1 cannot be degraded due to the dysfunctional proteases, and the accumulated PINK1 protein in the mitochondria phosphorylate its substrate, Parkin, which is a ubiquitin-ligating enzyme that is recruited to mitochondria under conditions of dysfunction, to ubiquitylate mitochondrial substrates[89,90]. Then the ubiquitylated mitochondria are enclosed into autophagosomes with the assistance of LC3B, followed by the fusion of lysosomes and autophagosomes, to subsequently digest the disabled mitochondria[89]. In this study, we extracted mitochondria from LMPt-treated cells and found that PINK1 and phosphorylated-Parkin (p-Parkin) were recruited to the mitochondria and that the mitochondria were significantly ubiquitinated, which occurred in a dose-dependent manner (Fig. 5K and Fig. S9G). These results prove that mitochondria were subjected to autophagy, in which the mitochondria were ubiquitinated for degradation. Further, mitophagy was also proved to be induced by LMPt in the tumor tissue derived from nude mice bearing pancreatic xenograft model (Fig. S9H).

To ascertain whether mitophagy is indeed the key to the pathological changes of the LMPt anti-cancer action, we utilized 3-MA and Baf-A1 which were reported to inhibit mitophagy[91−93], to assess whether the anti-cancer activity of LMPt could be inhibited in the addition of 3-MA and Baf-A1. Colony formation results show that the potent anti-cancer action was weakened in the presence of mitophagy inhibitors: 3-MA and Baf-A1 (Fig. 5L). Meanwhile, the autolysosome bubbles induced by LMPt were also withdrawn (Fig. 5M), indicating that mitophagy indeed plays an essential role in the LMPt induced anti-cancer activity in tumor cells.

In fact, after LMPt was processed by lysosomes, except for mitochondria, MPt as the degraded product also enter ER in unchanged metabolite (Fig. 4E and Fd). To determine whether ER damage was also occurred in LMPt treatment, we visualized the ER under TEM and found that the ER was dilated and distorted (Supporting Information Fig. S10I), suggesting possible ER stress. Correspondingly, we detected ER stress which would be activated in response to ER damage or dysfunction[94]. The ER stress-mediating pathways include PERK−eIF2α−ATF4, IRE−XBP1 and ATF6 pathways[94]. And only when the damage is severe, these response pathways would be activated continuously to trigger pro-apoptosis protein expression (CHOP, ATF4, cleaved-ATF6) to induce apoptosis[95−98]. To further evaluate whether ER damage was also involved in the LMPt anti-cancer effect, we detected ER stress pathways. Western blot results (Supporting Information Fig. S11A−S11D) showed that two of the three pathways were partly activated. In PERK−eIF2α−ATF4 pathway, PERK−eIF2α was activated, but the apoptotic effector ATF4 did not increase. Similar results were also observed in IRE−XBP1 pathway, where IRE1 was activated, but the effector protein, sliced XBP1 (XBP-1s) did not increase. The third pathway, ATF6, was not activated. These results revealed that although some ER stress pathways were activated, this activation might not be responsible for the anti-
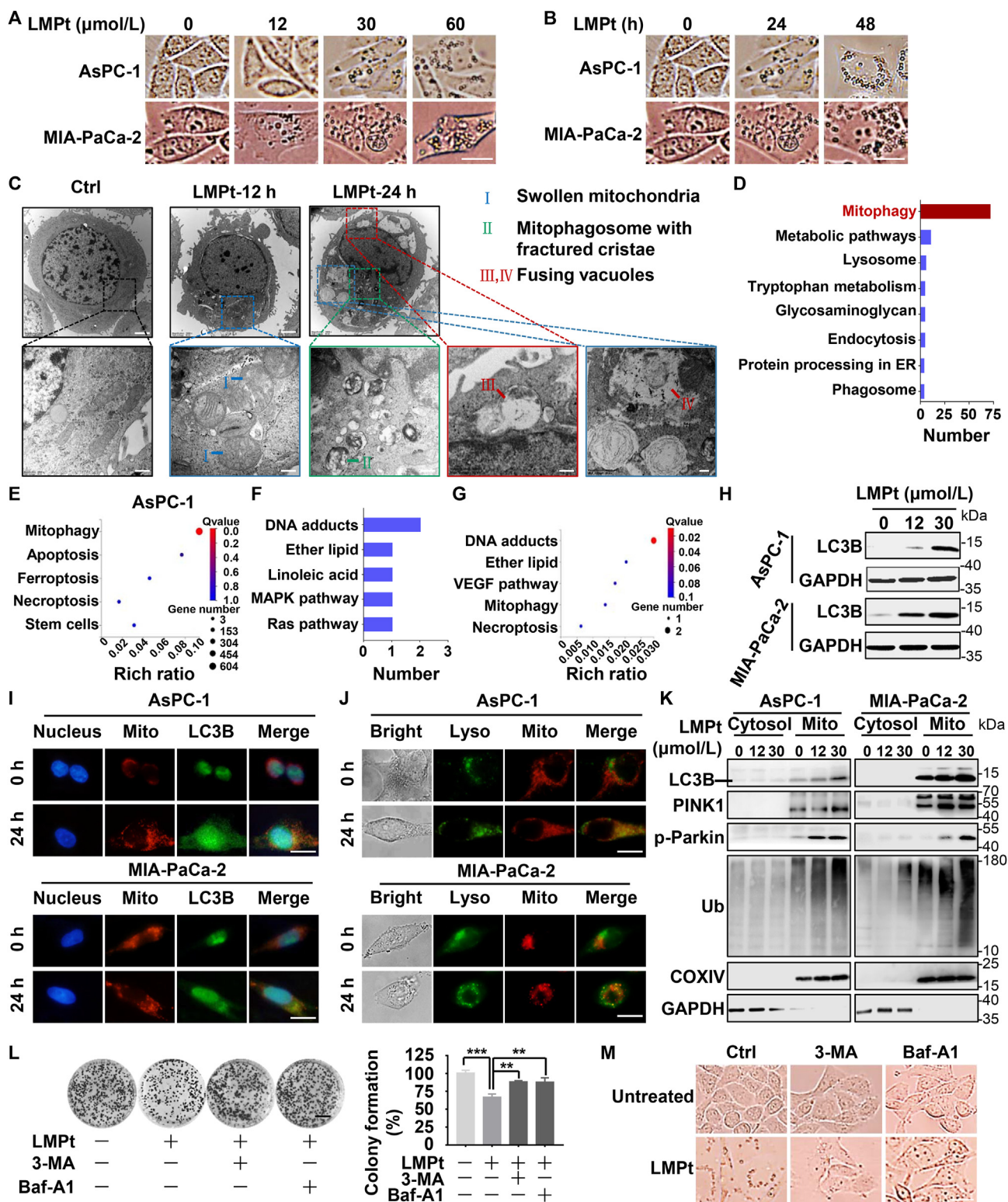
Figure 5 Instead of DNA damage, targeting mitochondria-induced mitophagy mediates anti-cancer action of LMPt. AsPC-1 and MIA-PaCa-2 cells were treated with indicated concentrations of LMPt for 24 h (A), or treated with 30 μmol/L LMPt for indicated time points (B), and cell morphology was observed with light microscopy. Scale bar, 20 μm. (C) AsPC-1 cells were treated with 30 μmol/L LMPt for 12 or 24 h and cells were observed with TEM. I: swollen mitochondria; II: mitophagosome with fractured cristae; III, IV: fusing vacuoles. Scale bar, up 2 μm and down 400 nm (enlarged images). (D) AsPC-1, MIA-PaCa-2 and BxPC-3 cells were treated with 30 μmol/L LMPt for 24 h and RNA was extracted for RNA-seq analysis with microarray. Gene Set Enrichment Analysis in the Molecular Signature Database was performed. Among differentially expressed genes (DEGs) from 3 comparison groups (Ctrl *vs.* LMPt for AsPC-1, MIA-PaCa-2 and BxPC-3 cells, |log2 Ratio| $\geq$ 1, *FDR* value $\leq$ 0.001), KEGG pathway functional classification was analyzed. (E) KEGG pathway enrichment of DEGs from Ctrl *vs.* LMPt for AsPC-

cancer effect of LMPt. Furthermore, we applied ER stress inhibitors, 4-PBA (1 mmol/L for 1 h[99]) and TUDCA (0.5 mmol/L for 2 h[100]) to perform the EdU proliferation assay, which revealed that ER stress inhibition did not reverse the proliferation inhibition caused by LMPt (Supporting Information Fig. S12).

Moreover, it was generally recognized that traditional platinum anti-cancer drugs, such as cisplatin and OXA, were reported to induce nuclear DNA damage to kill tumor cells. While as shown in Fig. 5C, the nucleus in the LMPt treated group stayed intact and almost no dense chromatin was observed, indicating little harm of LMPt to nucleus DNA. Meanwhile, we evaluated DNA damage *via* the DNA damage marker, γ-H2AX[58]. Western blot results confirm that LMPt did not induce obvious DNA damage at the effective concentrations *in vitro*, while OXA did at the same concentration (Supporting Information Fig. S13A). Additionally, total DNA was isolated from whole cell extracts and the ratio of Pt mass in DNA compared with that of the whole cell (Pt in DNA/whole cell) was calculated in LMPt or OXA treated cells (Fig. S13B). The results prove that at the same concentration, Pt in DNA/whole cell in OXA treated AsPC-1 and MIA-PaCA-2 cells were much higher than that of LMPt treated cells. This data indicate that OXA was more able to bind with DNA after cellular entry, while most of the intracellular LMPt did not bind to DNA, providing a possible explanation for the intact nucleus observed under TEM, as well as the less induction of γH2AX formation by LMPt. This further confirms that the nucleus was not the main target of LMPt after cell entry.

The above results demonstrated that LMPt induced mitophagy *via* activating PINK1−Parkin pathway to ubiquitinate mitochondria and further lysosomal degradation of mitochondria mediated by LC3B. When degradation was complete, the autophagic vacuoles would fuse with each other to form larger vacuoles, then the enlarged vacuoles would engulf smaller vacuoles, forming even larger vacuoles[85]. Although ER damage was also observed, this damage did not play the role key in LMPt's anti-cancer action. We supposed that the ER stress pathway was not continuously activated and led to cell apoptosis, or the role of damaged ER in cellular death was not equally vital as that of the mitochondria when the mitochondria was also damaged.

3.7. The enhanced degradation of POLG/TFAM by lon peptidase 1 (LONP1) leads to mitophagy via inhibiting mtDNA replication

Then, we explored the detailed mechanism of mitophagy after mitochondria were targeted by LMPt. Since most platinum agents usually bind to DNA to induce DNA break-mediated cell death, we speculated that LMPt might also disrupt or damage mtDNA. The classic mtDNA damage marker, 8-OHdG, was used to evaluate mtDNA damage[101,102]. The mtDNA damage response proteins FEN1, PCNA and RAD51 are usually activated to repair the damage and these proteins were regarded as the secondary

evidence of mtDNA damage[103]. The results showed that neither 8-OHdG (Fig. 6A) nor the repair proteins (Fig. 6B and Supporting Information Fig. S14A) were provoked, indicating that obvious mtDNA damage did not occur.

However, in mtDNA replication assay employing qRT-PCR, we found that the mtDNA copy number obviously decreased (Fig. 6C) in the presence of LMPt. Previous reports show that mtDNA encodes a plenty of oxidative phosphorylation proteins needed to maintain mitochondria function, and lack of mtDNA would lead to shortage of essential mitochondrial proteins, causing mitochondrial dysfunction and mitophagy[104−109]. Thus, we further explored the mechanism of mtDNA replication inhibition induced by LMPt and whether this mediated mitophagy and further inhibited proliferation.

Usually, during mtDNA replication, POLG, DNA polymerase gamma accessory subunit (POLG2), TFAM, single-stranded DNA-binding protein (mtSSB) and Twinkle were reported to play key roles[110−113]. In Western blot assay, after LMPt treatment, the levels of POLG, POLG2 and TFAM were significantly decreased *in vitro* and *in vivo* (Fig. 6D, Fig. S14B and S14C) among the above-mentioned mtDNA replication-associated proteins. Correspondingly, we overexpressed POLG, POLG2 and TFAM (Fig. 6E) followed by LMPt addition to assess whether overexpression of these proteins could abrogate the mtDNA replication barrier, and subsequent mitophagy and proliferation inhibition. Results revealed that only overexpression of POLG and TFAM could restore the LMPt-induced mtDNA replication blockade (Fig. 6F), mitophagy (Fig. 6G and Fig. S14D), and proliferation inhibition (Fig. 6H), indicating that the POLG and TFAM decrease mediated by LMPt was indispensable for the anti-pancreatic cancer efficacy of LMPt.

Subsequently, we further explored the potential mechanism of down-regulation of POLG and TFAM. Firstly, the mRNA level of *POLG* and *TFAM* did not decrease (Fig. S14E and S14F); indicating LMPt-induced TFAM and POLG decrease might not be a result of transcription modulation.

Accordingly, we focused on the protein degradation of POLG and TFAM. A mitochondrial protease, LONP1, located in mitochondrial matrix, usually acts to selectively degrade mitochondrial proteins[114−117] including mitochondrial POLG and TFAM[118−120]. Considering that LMPt dominantly targeted to mitochondria, we hypothesized that LMPt might facilitate the binding of POLG or TFAM with LONP1, thus promoting degradation of the two proteins. To test this, Co-Immunoprecipitation (Co-IP) assay was performed, and showed that LMPt indeed enhanced the interaction between POLG and TFAM with LONP1 (Fig. 6I). These results indicate that LMPt-induced expression decrease of POLG and TFAM was dependent on the enhanced interaction of POLG and TFAM with the LONP1 protease.

In conclusion, above results reveal that LMPt induced-mtDNA replication inhibition led to mitophagy through strengthening the binding of POLG and TFAM with the protease, LONP1.

---

1 cells. (F)−(G) RNA-seq analysis of AsPC-1 cells treated with MPt at its maximal solubility in cell culture medium for 24 h. (H) AsPC-1 and MIA-PaCa-2 cells were treated with LMPt for 24 h and LC3B were analyzed by Western blot. AsPC-1 and MIA-PaCa-2 cells were treated with LMPt for 24 h, colocalization of mitochondria (Mito) and LC3B (I) or lysosomes (Lyso) (J) was analyzed with immunofluorescence assay. Scale bar, 20 μm. (K) AsPC-1 and MIA-PaCa-2 cells were treated with indicated doses of LMPt for 24 h, then cytosol and Mito were extracted for indicated protein analysis by Western blot. (L) AsPC-1 cells were seeded in 6-well plate at 1000 cells/well and treated with 1.6 μmol/L LMPt with or without 3-MA (50 μmol/L) and Baf-A1 (2 nmol/L) for colony formation assay. Scale bar, 8 mm. Colony formation rates are shown in the histogram. **$P < 0.01$, ***$P < 0.001$. The data are shown as mean ± SD ($n = 3$) (M) Cellular morphology at 24 h after treatment with 1.6 μmol/L LMPt with or without 3-MA (50 μmol/L) and Baf-A1 (2 nmol/L). Scale bar, 20 μm.
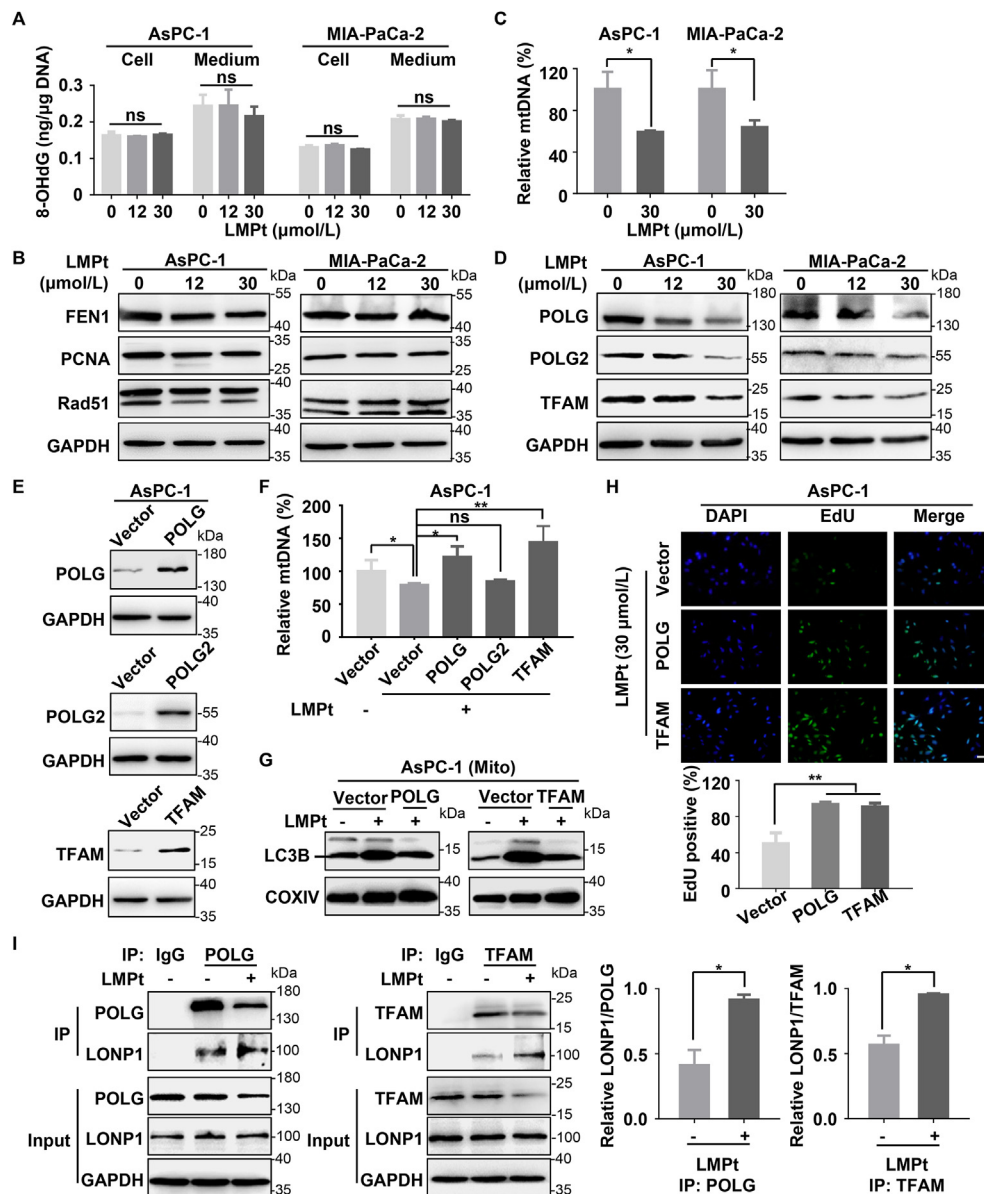
Figure 6 mtDNA replication inhibition leads to mitophagy *via* the strengthened binding of LONP1 with POLG/TFAM in the presence of LMPt. AsPC-1 and MIA-PaCa-2 cells were treated with the indicated doses of LMPt for 24 h, and mtDNA damage marker 8-OHdG in DNA and medium were detected (A), mtDNA damage repair proteins were analyzed (B), mtDNA copy numbers were analyzed with qRT-PCR (C) and POLG, POLG2 and TFAM were analyzed (D). (E) AsPC-1 cells were transfected with POLG, POLG2 and TFAM, and indicated proteins were analyzed with Western blot. (F) AsPC-1 cells were transfected with POLG, POLG2 and TFAM with or without 30 μmol/L LMPt for 24 h, and mtDNA copy numbers were determined by qRT-PCR. AsPC-1 cells were transfected with POLG and TFAM with or without 30 μmol/L LMPt for 24 h and mitochondria (Mito) were extracted for LC3B detection with Western blot (G), and proliferation was evaluated with EdU assay, scale bar, 40 μm (H). (I) AsPC-1 cells were treated with 30 μmol/L LMPt for 24 h and POLG or TFAM was immunoprecipitated for LONP1 detection by immunoblot. ns, no significant, *$P < 0.05$, **$P < 0.01$. All the data are shown as mean ± SD ($n = 3$).

3.8. POLG and TFAM are the prognosis markers of pancreatic cancer and promote pancreatic cancer growth via inhibiting mitophagy

Numerous previous reports showed that POLG or TFAM play essential roles in mtDNA replication, but their roles in tumor and mitophagy were not reported. Our above results show that LMPt-induced down regulation of POLG and TFAM resulting in mitophagy-mediated growth inhibition, suggesting that POLG and TFAM may be potential anti-cancer targets. Thus, we further

explored the roles of POLG and TFAM in tumor development and mitophagy. First, mRNA levels of *POLG* and *TFAM* in pancreatic cancer tissues and corresponding normal tissues were compared, based on various datasets (Logsdon Pancreas, Badea Pancreas, Pei Pancreas, Buchholz Pancreas, Ishikawa Pancreas and Segara Pancreas) from publicly available Oncomine database (www.oncomine.org). Results reveal that in each dataset, the mRNA level of either *POLG* or *TFAM* was significantly higher in pancreatic cancer tissue than that of corresponding normal pancreas tissue (Fig. 7A). Moreover, immunohistochemistry results from the publicly
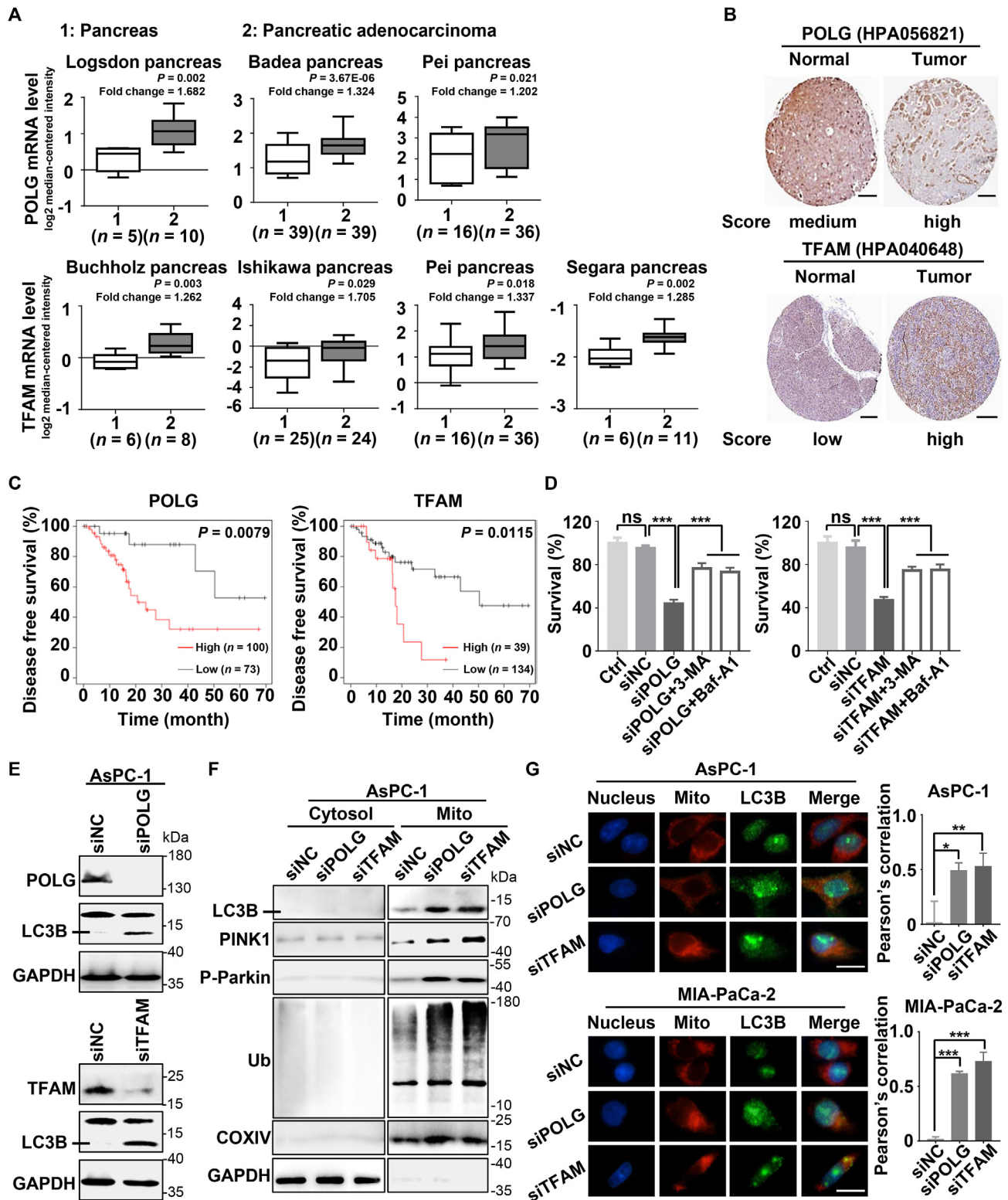
Figure 7 POLG and TFAM are prognostic markers of pancreatic cancer and promote pancreatic cancer growth *via* inhibiting mitophagy. (A) The mRNA levels of *POLG* and *TFAM* in pancreatic adenocarcinoma and the corresponding adjacent normal tissues were assessed from the publicly available Oncomine database (www.oncomine.org). Logsdon Pancreas, Badea Pancreas, Pei Pancreas, Buchholz Pancreas, Ishikawa Pancreas and Segara Pancreas represent 6 different Oncomine databases. 1: Pancreas; 2: Pancreatic Adenocarcinoma. (B) Immunohistochemistry (IHC) of POLG and TFAM protein level in pancreatic adenocarcinoma and adjacent normal tissues, assessed from the publicly available The Human Protein Atlas database (www.proteinatlas.org). Scale bar, 200 μm. (C) Disease-free survival of patients based on POLG and TFAM expression. Kaplan−Meier curves were constructed to observe the survival of patients with high and low POLG and TFAM expression based on Kaplan−Meier Plotter database (http://kmplot.com/analysis). Patients with POLG and TFAM expression within the top 50% were chosen as the

available "the Human Protein Atlas database" also showed that the protein level of both POLG and TFAM was upregulated in human pancreatic cancer tissues compared to corresponding peritumoral tissues (Fig. 7B). Additionally, two datasets analysis showed that the level of POLG and TFAM was negatively correlated with survival (Fig. 7C). The above results indicate that POLG and TFAM was highly expressed in pancreatic cancer tissues and might act as prognostic markers for pancreatic cancer.

Then, we investigated role of POLG and TFAM in tumor development. First, we silenced POLG and TFAM and observed cell proliferation. Results show cell proliferation was both suppressed in POLG and TFAM knockdown cells, indicating POLG and TFAM could promote pancreatic cancer cell proliferation (Fig. 7D, first three columns in the two histograms).

Furthermore, we explored the pro-cancer mechanism of POLG and TFAM. Based on our above research, down-regulation of POLG and TFAM contributed to LMPt-induced mitophagy and subsequently proliferation inhibition, we hypothesized that depletion of POLG and TFAM might inhibit cellular growth *via* mitophagy in cancer cells. Consequently, we silenced POLG and TFAM, and found that the LC3B level increased, as expected (Fig. 7E and Supporting Information Fig. S15A). Also, the increased LC3B was located in the mitochondria (Fig. 7F and Fig. S15B). We then exacted mitochondria from POLG and TFAM silenced cells, and found that LC3, PINK1 and p-Parkin proteins, which contributed to mitophagy *via* ubiquitinating mitochondria, were recruited to the mitochondria. Meanwhile, we observed obvious mitochondrial ubiquitylation in these conditions as well (Fig. 7F and Fig. S15B). What's more, an increase of colocalization (indicated by yellow puncta) of mitochondria (red puncta) with increased LC3B in the cytoplasm (green puncta) was also observed by immunofluorescence, indicating an accelerated mitophagosome formation (Fig. 7G).

Next, we applied mitophagy inhibitors, 3-MA and Baf-A1, to detect whether mitophagy was involved in anti-cancer action in down-regulated POLG and TFAM cells. These results show that mitophagy block indeed restored POLG and TFAM-silenced-induced growth inhibition (Fig. 7D, last two columns in the two histograms), indicating that POLG and TFAM promote proliferation *via* antagonizing mitophagy. Our results are the first to clarify the antagonistic action of POLG and TFAM on mitophagy and their pro-cancer roles. Furthermore, we demonstrate that POLG and TFAM facilitate pancreatic cancer proliferation *via* mitophagy inhibition.

4. Discussion

Liposomal formulations of anti-cancer drugs have shown remarkable advantages in cancer chemotherapy due to their high efficiency and low toxicity, such as Doxil, Onivyde, and Lipusu. No platinum-based nano-preparation has been approved so far, although platinum-based chemotherapeutic agents have been used in clinical practice for more than 40 years. MPt is a broad-spectrum anti-cancer drug and is currently applied for local treatment in MPt/lipiodol suspension due to its poor solubility. Therefore, in our previous studies, LMPt was successfully constructed and developed for intravenous systemic administration in the treatment of a variety of cancers[29].

For the *in vivo* evaluation, 30 mg/kg was chosen as an administration dosage of LMPt for the following reason. In our preliminary assays showed that the maximal tolerated dose of LMPt was 50 mg/kg, and under this concentration for a single dose, LMPt did not induce toxicity, but the repeated administration induced obvious weight loss. Further assay demonstrated that 30 mg/kg was the appropriate dosage for LMPt, because under this dose the repeated administration did not induce toxicity including the regular Pt-associated toxicities.

In this study, we found the highlight of LMPt that it not only inhibited the proliferation of GEM-S pancreatic cancer cells, but also had a similar effect on GEM-R cells. The preponderance of the anti-cancer effect of LMPt was evident, especially at 24 h, in comparison with that of OXA, the structural analog of MPt, indicating a more rapid effect. This finding may be beneficial for patients requiring rapid tumor shrinkage before surgery. The LMPt-induced rapid entry of Pt may be responsible for the rapid effect due to the higher affinity of the liposome and cell membrane. Importantly, in *in vivo* assays, we did not observe toxicities especially peripheral neurotoxicity or myelosuppression, which are the major barriers in platinum application, suggesting another advantage conferred by liposomes through their ability to passively target to the tumor.

Through mechanistic study, we depicted a complete efficacy pathway of LMPt, including cellular entry, intracellular transportation, and processing, targeting metabolites, subcellular targeting sites, and pathological changes of targeting sites, as well as show LMPt metabolites induced mitophagy-dependent cell death after targeting the mitochondria. Mechanistic analysis revealed several findings worthy of particular focus.

First, we elucidated the reason why anti-cancer efficacy of LMPt was different in various cells, which was related to the difference in its cellular entry rate, as determined by the initiated endocytosis pathways. Current reports regarding cellular entry of nanoparticles usually only focus on the pathways involved in the endocytosis process, but few insightfully elucidate in what case which endocytosis pathways are involved and the interaction as well as switching of these endocytosis pathways during nanoparticle entry. In our study, we initially found that Cav-1 level played a key role, and when it was high, Cav-1-mediated endocytosis facilitated LMPt entry. While in low-Cav-1 cells, macropinocytosis and Cav-1 induced by LMPt contributed to LMPt endocytosis together. Additionally, in high-Cav-1 cells, LMPt was transported into cells faster and exerted better anti-cancer efficacy. This finding implies that patients with higher Cav-1 expression level may benefit more from LMPt treatment than those with low Cav-1 expression level. These findings will facilitate further studies on LMPt development and administration.

---

high POLG and TFAM group, and those with POLG and TFAM expression in the bottom 50% were chosen as the low POLG and TFAM group. Differences were evaluated by a log-rank (Mantel−Cox) test. (D) Cellular viability was detected by MTT assay for POLG- or TFAM-depleted AsPC-1 cells treated with or without 3-MA (50 μmol/L) and Baf-A1 (2 nmol/L). (E) AsPC-1 cells were transfected with siNC, siPOLG or siTFAM and LC3B was analyzed. (F) AsPC-1 cells were transfected with siNC, siPOLG or siTFAM and mitochondria (Mito) were extracted for mitophagy-related proteins analysis. (G) Colocalization of Mito with the increased LC3B in AsPC-1 and MIA-PaCa-2 cells after knockdown of POLG and TFAM. Scale bar, 20 μm. Pearson correlation coefficients were analyzed by ImageJ. ns, no significant. *$P < 0.05$, **$P < 0.01$, ***$P < 0.001$. The data are shown as mean $\pm$ SD ($n = 3$).
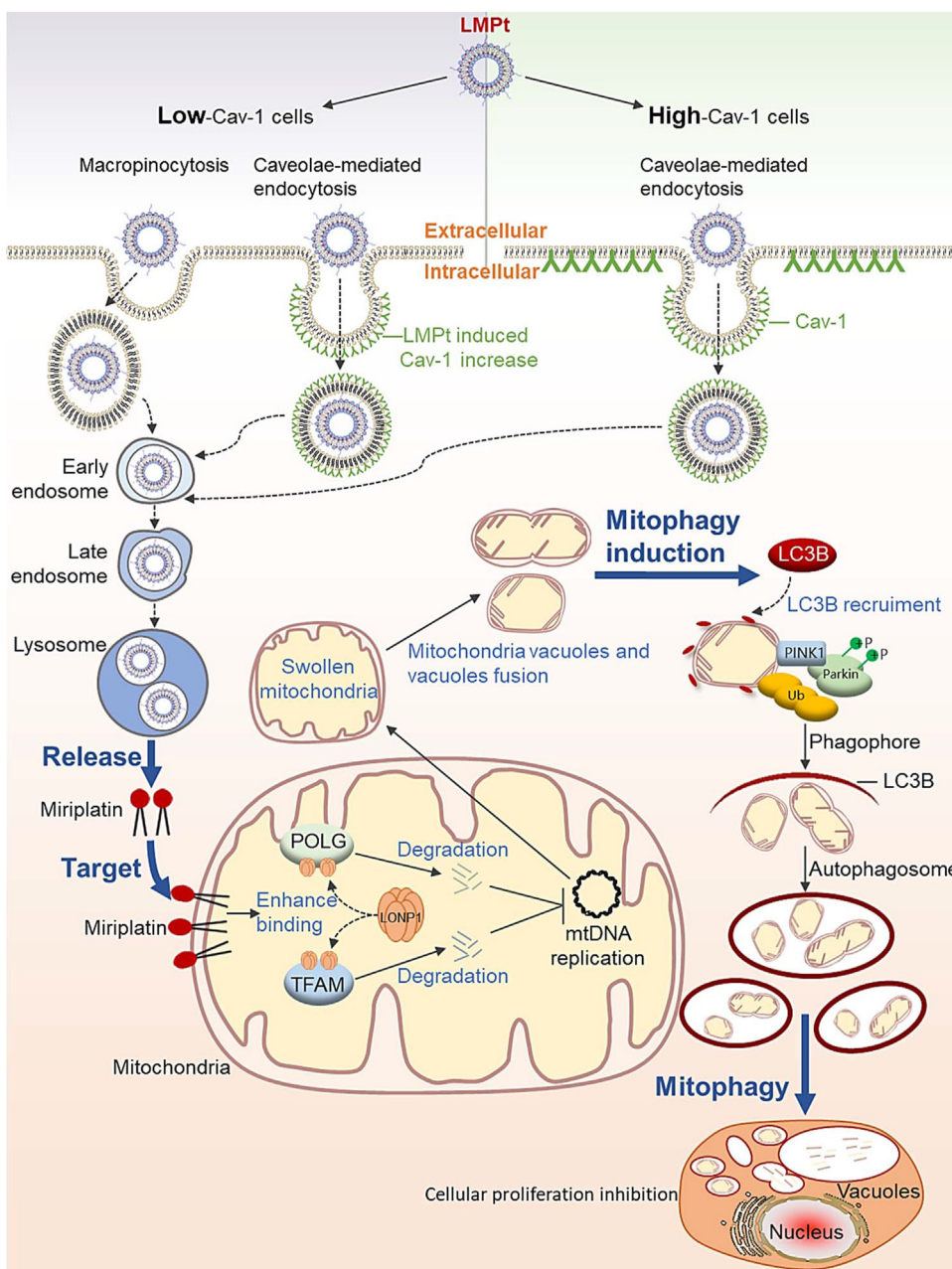
Figure 8 Mechanism schematic diagram of LMPt involving cellular entry and anti-cancer effect in pancreatic cancer cells. LMPt enters cells *via* caveolae-mediated endocytosis and macropinocytosis, and Cav-1 level determines the switch of endocytosis pathways. In high Cav-1 cells, only Cav-1 mediates LMPt endocytosis and in low Cav-1 cells, macropinocytosis and LMPt-induced Cav-1 contribute to LMPt endocytosis together. After endosome−lysosome processing, in unchanged metabolite, MPt is released and targets mitochondria to enhance binding of mitochondria protease LONP1 with POLG and TFAM (key players of mtDNA replication) to degrade POLG and TFAM. Then *via* PINK1−Parkin axis mitophagy is induced based on POLG and TFAM degradation-initiated mtDNA replication block.

Second, we found that the dominant intracellular target of LMPt was the mitochondria. We speculated that the potential reason for this targeting was similar to the theory of the LMPt preparation. The fatty acid chains of MPt and phospholipids are similar in structure and polarity, thus, they are matched for incorporation into the liposome layer to form LMPt. Similarly, lipids consisting of biological membranes (for example, the membranes of cellular organelles) also have two long fatty acid chains (Supporting Information Fig. S16), which resemble MPt in structure and polarity. Therefore, MPt, released in unchanged

metabolite from LMPt after lysosome digestion, is more readily able to interact with biological membranes and thereafter enter membrane-bound organelles. Among membrane-bound organelles, mitochondria are large, numerous, and vital to cellular survival, making mitochondria a more important targeting organelle of LMPt. Further results also supported this hypothesis, as mitophagy was induced after LMPt treatment. Additionally, previous studies on the anti-cancer mechanisms of platinum have also demonstrated that most platinum agents primarily target nuclear DNA to exhibit anti-cancer

efficacy[58,121], which is similar to MPt's mechanism. While our results revealed a totally novel anti-tumor mechanism of MPt after encapsulation into liposomes. This novel mechanism may provide more possibilities for combination therapies.

Third, in LMPt-induced mitophagy, we found that POLG and TFAM played key roles. In previous reports, POLG and TFAM were only elucidated to be involved in mtDNA replication, whereas very few reports noted their role in mitophagy, especially in tumor cells. In this study, we found that POLG and TFAM suppressed mitophagy by contributing to mtDNA replication. This discovery supplemented the role of POLG and TFAM in the network of mtDNA function maintenance and mitophagy regulation. Furthermore, POLG and TFAM may act as tumor prognosis biomarkers and potential tumor-inhibiting targets by promoting mitophagy.

Finally, the anti-cancer mechanism of LMPt was found entirely different from that of MPt (although activity is poor) in the following aspects. In cellular entry, MPt did not depend on the pathways mediating LMPt entry and only a small amount of MPt could enter cells. In organelle targeting, the major target of LMPt is mitochondria, while the target of MPt is DNA. In molecular pathways changing, LMPt induced significant changes in mitophagy-associated pathway, but MPt only induced slight change in the DNA adduct-leading effect pathway. There is a possible reason for the different targets of LMPt and MPt. As reported previously, nanoparticles gain cellular entry primarily through endocytosis, whereas small-molecule drugs enter cells mainly through passive diffusion or active transport. Different cell entry pathways lead to different intracellular trafficking fates, cellular metabolism of active ingredients, subsequent organelle localization, and pharmacological activity of anti-cancer agents, which may lead to different action mechanisms[67,122,123]. In our study, we observed that the transporters of LMPt and MPt were different. Thus, we speculated that it may be the different transporters that mediated the different cellular localization and metabolism of the active ingredient, as well as the subsequent different cellular targets and actions between LMPt and MPt. Additionally, it was demonstrated that, for another formulation of MPt, MPt/lipoidol, apoptosis was the key anti-tumor mechanism[27,54,56,57]. All these studies and analysis indicate that liposomal MPt possesses characteristic anti-cancer mechanism different from that of MPt or MPt/lipoidol, and it is the liposomal formulation that endows MPt with a distinct anti-cancer mechanism and superior pharmacological activity.

In fact, further studies are required to clarify some issues, such as the molecular mechanism involved in the fusion of mitophagy empty bubbles to form large-sized bubbles and how LMPt enters the mitochondria. Clarifications of these unsolved issues will be the primary focus of our next study.

5. Conclusions

LMPt is a novel and auto-assembly platinum-based liposome prepared employing the structure character of MPt, and could exert excellent action. Its novel and unique endocytosis mechanism based on Cav-1 endogenous level would offer clinical administration guidance to predict the patients that would gain the maximize benefit from LMPt treatment. Additionally, our research is the first to disclosed mitochondria as the major target of platinum after preparing into liposome formulation, which is virtually different from the traditional view in which the dominant targeting

site of most platinum is nuclear DNA. These results broaden the potential targets of platinum anti-cancer agents. This discovery brings help for the anti-cancer drug combination based on action mechanism (Fig. 8). Above all, low toxicity, strong anti-cancer action and characteristic anti-cancer mechanism made LMPt a promising candidate as a clinical anti-pancreatic cancer agent.

Author contributions

Wuli Zhao: conceptualization, writing-review & editing, supervision. Rongguang Shao: conceptualization, supervision. Guimin Xia: funding acquisition, conceptualization, supervision. Xiaowei Wang: methodology, data curation, software, writing-original draft. Mengyan Wang and Meilian Cai: validation.

Conflicts of interest

The authors declare no conflicts of interest.

Appendix A. Supporting information

Supporting data to this article can be found online at https://doi.org/10.1016/j.apsb.2023.07.009.

References

1. Globocan W. *Estimated cancer incidence and mortality worldwide in*. 2020. Available from: https://gco.iarc.fr/today/data/factsheets/cancers/13-Pancreas-fact-sheet.pdf.
2. Binenbaum Y, Na'ara S, Gil Z. Gemcitabine resistance in pancreatic ductal adenocarcinoma. *Drug Resist Updates* 2015;**23**:55−68.
3. Fu Y, Ricciardiello F, Yang G, Qiu J, Huang H, Xiao J, et al. The role of mitochondria in the chemoresistance of pancreatic cancer cells. *Cells* 2021;**10**:497.
4. Nevala-Plagemann C, Hidalgo M, Garrido-Laguna I. From state-of-the-art treatments to novel therapies for advanced-stage pancreatic cancer. *Nat Rev Clin Oncol* 2020;**17**:108−23.
5. Xiong W, Qi L, Jiang N, Zhao Q, Chen L, Jiang X, et al. Metformin liposome-mediated PD-L1 downregulation for amplifying the photodynamic immunotherapy efficacy. *ACS Appl Mater Interfaces* 2021;**13**:8026−41.
6. Guimaraes D, Cavaco-Paulo A, Nogueira E. Design of liposomes as drug delivery system for therapeutic applications. *Int J Pharm* 2021;**601**:120571.
7. Bozzuto G, Molinari A. Liposomes as nanomedical devices. *Int J Nanomed* 2015;**10**:975−99.
8. Biswas S, Torchilin VP. Nanopreparations for organelle-specific delivery in cancer. *Adv Drug Deliv Rev* 2014;**66**:26−41.
9. Moosavian SA, Bianconi V, Pirro M, Sahebkar A. Challenges and pitfalls in the development of liposomal delivery systems for cancer therapy. *Semin Cancer Biol* 2021;**69**:337−48.

10. Hong DS, Kang YK, Borad M, Sachdev J, Ejadi S, Lim HY, et al. Phase 1 study of mrx34, a liposomal mir-34a mimic, in patients with advanced solid tumours. *Br J Cancer* 2020;**122**:1630−7.

11. Chunjuan Zheng WL, Liu Yu, Chen Jiashe, Deng Hui, Zhou Zaigang, Shen Jianliang. Killing three birds with one stone: multi-stage metabolic regulation mediated by clinically useable berberine liposome to overcome photodynamic immunotherapy resistance. *Chem Eng J* 2023;**454**:140164.

12. Gao A, Hu XL, Saeed M, Chen BF, Li YP, Yu HJ. Overview of recent advances in liposomal nanoparticle-based cancer immunotherapy. *Acta Pharmacol Sin* 2019;**40**:1129−37.

13. Zhong HH, Wang HY, Li J, Huang YZ. Trail-based gene delivery and therapeutic strategies. *Acta Pharmacol Sin* 2019;**40**:1373−85.

14. Zhong HH, Wang HY, Gao J, Huang YZ, Gao A, Hu XL, et al. Publisher correction: 'Trail-based gene delivery and therapeutic strategies' and 'overview of recent advances in liposomal nanoparticle-based cancer immunotherapy'. *Acta Pharmacol Sin* 2021;**42**:843.

15. Hu Chuan, Song Yujun, Zhang Yiwei, He Siqin, Liu Xueying, Yang Xiaotong, et al. Sequential delivery of PD-1/PD-L1 blockade peptide and IDO inhibitor for immunosuppressive microenvironment remodeling *via* an MMP-2 responsive dual-targeting liposome. *Acta Pharm Sin B* 2023;**13**:2176−87.

16. He Y, Fang Y, Zhang M, Zhao Y, Tu B, Shi M, et al. Remodeling "cold" tumor immune microenvironment *via* epigenetic-based therapy using targeted liposomes with *in situ* formed albumin corona. *Acta Pharm Sin B* 2022;**12**:2057−73.

17. Zhou Z, Liu Y, Jiang X, Zheng C, Luo W, Xiang X, et al. Metformin modified chitosan as a multi-functional adjuvant to enhance cisplatin-based tumor chemotherapy efficacy. *Int J Biol Macromol* 2023;**224**:797−809.

18. Li Y, Qian D, Lin HP, Xie J, Yang P, Maddy D, et al. Nanoparticle-delivered miriplatin ultrasmall dots suppress triple negative breast cancer lung metastasis by targeting circulating tumor cells. *J Contr Release* 2021;**329**:833−46.

19. Zalba S, Garrido MJ. Liposomes, a promising strategy for clinical application of platinum derivatives. *Expet Opin Drug Deliv* 2013;**10**:829−44.

20. Seetharamu N, Kim E, Hochster H, Martin F, Muggia F. Phase II study of liposomal cisplatin (SPI-77) in platinum-sensitive recurrences of ovarian cancer. *Anticancer Res* 2010;**30**:541−5.

21. Stathopoulos GP, Boulikas T. Lipoplatin formulation review article. *J Drug Deliv* 2012;**2012**:581363.

22. Stathopoulos GP, Boulikas T, Kourvetaris A, Stathopoulos J. Liposomal oxaliplatin in the treatment of advanced cancer: a phase I study. *Anticancer Res* 2006;**26**:1489−93.

23. Wang D, Feng W, Wang X, Lin D, Wang X, Guo X, et al. Promoted antitumor therapy on pancreatic cancer by a novel recombinant human albumin-bound miriplatin nanoparticle. *Eur J Pharmaceut Sci* 2021;**167**:106000.

24. Duan X, He C, Kron SJ, Lin W. Nanoparticle formulations of cisplatin for cancer therapy. *Wiley Interdiscip Rev Nanomed Nanobiotechnol* 2016;**8**:776−91.

25. Oberoi HS, Nukolova NV, Kabanov AV, Bronich TK. Nanocarriers for delivery of platinum anticancer drugs. *Adv Drug Deliv Rev* 2013;**65**:1667−85.

26. Ikeda K. Recent advances in medical management of hepatocellular carcinoma. *Hepatol Res* 2019;**49**:14−32.

27. Tanaka KT, Shimakura J, Hanada M. Development of miriplatin, a novel antitumor platinum for hepatocellular carcinoma. *Sumitomo Kagaku* 2011:39−48.

28. Yasui D, Yamane A, Itoh H, Kobayashi M, Kumita SI. *In vivo* evaluation of a monodisperse solid-in-oil-in-water miriplatin/lipiodol emulsion in transcatheter arterial chemoembolization using a rabbit VX$_2$ tumor model. *PLoS One* 2020;**15**:e0222553.

29. Liu S, Li Y, Wang X, Ma J, Zhang L, Xia G. Preparation, characterization, and antitumor activities of miriplatin-loaded liposomes. *J Pharm Sci* 2016;**105**:78−87.

30. Steigenberger J, Verleysen Y, Geudens N, Martins JC, Heerklotz H. The optimal lipid chain length of a membrane-permeabilizing lipopeptide results from the balance of membrane partitioning and local damage. *Front Microbiol* 2021;**12**:669709.

31. Hiwale AA, Voshavar C, Dharmalingam P, Dhayani A, Mukthavaram R, Nadella R, et al. Scaling the effect of hydrophobic chain length on gene transfer properties of di-alkyl, di-hydroxy ethylammonium chloride based cationic amphiphiles. *RSC Adv* 2017;**7**:25398−405.

32. Zhang H, Wu P, Wang Y, Cao J. Affinity of miriplatin to human serum albumin and its effect on protein structure and stability. *Int J Biol Macromol* 2016;**92**:593−9.

33. Aramaki T, Moriguchi M, Bekku E, Asakura K, Sawada A, Endo M. Comparison of epirubicin hydrochloride and miriplatin hydrate as anticancer agents for transcatheter arterial chemoembolization of hepatocellular carcinoma. *Hepatol Res* 2013;**43**:475−80.

34. Vichai V, Kirtikara K. Sulforhodamine B colorimetric assay for cytotoxicity screening. *Nat Protoc* 2006;**1**:1112−6.

35. Liu H, Zhao WL, Wang JP, Xin BM, Shao RG. EBP50 suppresses the proliferation of MCF-7 human breast cancer cells *via* promoting beclin-1/p62-mediated lysosomal degradation of c-myc. *Acta Pharmacol Sin* 2018;**39**:1347−58.

36. English SG, Sandoval-Herrera NI, Bishop CA, Cartwright M, Maisonneuve F, Elliott JE, et al. Neonicotinoid pesticides exert metabolic effects on avian pollinators. *Sci Rep* 2021;**11**:2914.

37. Sattabongkot J, Suansomjit C, Nguitragool W, Sirichaisinthop J, Warit S, Tiensuwan M, et al. Prevalence of asymptomatic plasmodium infections with sub-microscopic parasite densities in the northwestern border of Thailand: a potential threat to malaria elimination. *Malar J* 2018;**17**:329.

38. Zhang Y, Li C, Qin Y, Cepparulo P, Millman M, Chopp M, et al. Small extracellular vesicles ameliorate peripheral neuropathy and enhance chemotherapy of oxaliplatin on ovarian cancer. *J Extracell Vesicles* 2021;**10**:12073.

39. Wang L, Chopp M, Jia L, Lu X, Szalad A, Zhang Y, et al. Therapeutic benefit of extended thymosin β4 treatment is independent of blood glucose level in mice with diabetic peripheral neuropathy. *J Diabetes Res* 2015;**2015**:173656.

40. Wang L, Chopp M, Szalad A, Jia L, Lu X, Lu M, et al. Sildenafil ameliorates long term peripheral neuropathy in type II diabetic mice. *PLoS One* 2015;**10**:e0118134.

41. Cui Y, Onozawa M, Garber HR, Samsel L, Wang Z, McCoy JP, et al. Thymic expression of a T-cell receptor targeting a tumor-associated antigen coexpressed in the thymus induces T-ALL. *Blood* 2015;**125**:2958−67.

42. Vaseghi H, Houshmand M, Jadali Z. Increased levels of mitochondrial DNA copy number in patients with vitiligo. *Clin Exp Dermatol* 2017;**42**:749−54.

43. Yoshida K, Toden S, Ravindranathan P, Han H, Goel A. Curcumin sensitizes pancreatic cancer cells to gemcitabine by attenuating PRC$_2$ subunit EZH$_2$, and the lncRNA PVT$_1$ expression. *Carcinogenesis* 2017;**38**:1036−46.

44. Cao J, Yang J, Ramachandran V, Arumugam T, Deng D, Li Z, et al. TM$_4$SF$_1$ promotes gemcitabine resistance of pancreatic cancer *in vitro* and *in vivo*. *PLoS One* 2015;**10**:e0144969.

45. Rejiba S, Bigand C, Parmentier C, Hajri A. Gemcitabine-based chemogene therapy for pancreatic cancer using Ad-dCK::UMK GDEPT and TS/RR siRNA strategies. *Neoplasia* 2009;**11**:637−50.

46. Franken NA, Rodermond HM, Stap J, Haveman J, van Bree C. Clonogenic assay of cells *in vitro*. *Nat Protoc* 2006;**1**:2315−9.

47. Okada M, Shi YB. Cell proliferation analysis during xenopus metamorphosis: using 5-ethynyl-2-deoxyuridine (EdU) to stain proliferating intestinal cells. *Cold Spring Harb Protoc* 2017;**2017**:pdb.prot097717.

48. Kumar P, Kulkarni A, Sharma M, Rao PN, Reddy DN. Favipiravir-induced liver injury in patients with coronavirus disease 2019. *J Clin Transl Hepatol* 2021;**9**:276−8.

49. Hermel DJ, Du EZ, Lin R, Frenette CT, Sigal DS. Checkpoint inhibition in the treatment of unresectable, advanced lymphoepithelioma-like hepatocellular carcinoma. *J Clin Transl Hepatol* 2021;**9**:265−8.

50. Kawashiri T, Mine K, Kobayashi D, Inoue M, Ushio S, Uchida M, et al. Therapeutic agents for oxaliplatin-induced peripheral neuropathy; experimental and clinical evidence. *Int J Mol Sci* 2021;**22**:1393.

51. Kang L, Tian Y, Xu S, Chen H. Oxaliplatin-induced peripheral neuropathy: clinical features, mechanisms, prevention and treatment. *J Neurol* 2021;**268**:3269−82.

52. Tanak K, Kunimatsu T, Shimakura J, Hanada M. Development of miriplatin, a novel antitumor platinum for hepatocellular carcinoma. *Sumitomo Kagaku RD Rep* 2011;**1**:11−2.

53. Hall MD, Telma KA, Chang KE, Lee TD, Madigan JP, Lloyd JR, et al. Say no to DMSO: dimethylsulfoxide inactivates cisplatin, carboplatin, and other platinum complexes. *Cancer Res* 2014;**74**: 3913−22.

54. Kishimoto S, Miyazawa K, Fukushima S, Takeuchi Y. *In vitro* antitumor activity, intracellular accumulation, and DNA adduct formation of *cis*-[((1*R*,2*R*)-1,2-cyclohexanediamine-*N,N'*)bis(myristato)] platinum (II) suspended in lipiodol. *Jpn J Cancer Res* 2000;**91**: 99−104.

55. Kishimoto S, Noguchi T, Yamaoka T, Fukushima S, Takeuchi Y. *In vitro* release of sm-11355, *cis*[((1*R*,2*R*)-1,2-cyclohexanediamine-*N,N'*)bis(myristato)] platinum(II) suspended in lipiodol. *Biol Pharm Bull* 2000;**23**:637−40.

56. Hanada M, Baba A, Tsutsumishita Y, Noguchi T, Yamaoka T. Intra-hepatic arterial administration with miriplatin suspended in an oily lymphographic agent inhibits the growth of human hepatoma cells orthotopically implanted in nude rats. *Cancer Sci* 2009;**100**:189−94.

57. Hanada M, Baba A, Tsutsumishita Y, Noguchi T, Yamaoka T, Chiba N, et al. Intra-hepatic arterial administration with miriplatin suspended in an oily lymphographic agent inhibits the growth of tumors implanted in rat livers by inducing platinum−DNA adducts to form and massive apoptosis. *Cancer Chemother Pharmacol* 2009;**64**: 473−83.

58. Jung Y, Lippard SJ. Direct cellular responses to platinum-induced DNA damage. *Chem Rev* 2007;**107**:1387−407.

59. Khoury A, Deo KM, Aldrich-Wright JR. Recent advances in platinum-based chemotherapeutics that exhibit inhibitory and targeted mechanisms of action. *J Inorg Biochem* 2020;**207**:111070.

60. Zhang J, Qin M, Yang D, Yuan L, Zou X, Dai W, et al. Nanoprotein interaction atlas reveals the transport pathway of gold nanoparticles across epithelium and its association with Wnt/*β*-Catenin signaling. *ACS Nano* 2021;**15**:17977−97.

61. Debnath K, Pal S, Jana NR. Chemically designed nanoscale materials for controlling cellular processes. *Acc Chem Res* 2021;**54**:2916−27.

62. Qin X, Yang C, Xu H, Zhang R, Zhang D, Tu J, et al. Cell-derived biogenetic gold nanoparticles for sensitizing radiotherapy and boosting immune response against cancer. *Small* 2021;**17**:e2103984.

63. Valinezhad Sani F, Palizban A, Mosaffa F, Jamialahmadi K. Glucosamine reverses drug resistance in MRP2 overexpressing ovarian cancer cells. *Eur J Pharmacol* 2020;**868**:172883.

64. Zou M, Hu X, Xu B, Tong T, Jing Y, Xi L, et al. Glutathione stransferase isozyme alpha 1 is predominantly involved in the cisplatin resistance of common types of solid cancer. *Oncol Rep* 2019;**41**:989−98.

65. Petruzzelli R, Polishchuk RS. Activity and trafficking of copper-transporting atpases in tumor development and defense against platinum-based drugs. *Cells* 2019;**8**:1080.

66. Nakayama K, Kanzaki A, Terada K, Mutoh M, Ogawa K, Sugiyama T, et al. Prognostic value of the Cu-transporting atpase in ovarian carcinoma patients receiving cisplatin-based chemotherapy. *Clin Cancer Res* 2004;**10**:2804−11.

67. Wang X, Qiu Y, Wang M, Zhang C, Zhang T, Zhou H, et al. Endocytosis and organelle targeting of nanomedicines in cancer therapy. *Int J Nanomed* 2020;**15**:9447−67.

68. Manzanares D, Cena V. Endocytosis: the nanoparticle and submicron nanocompounds gateway into the cell. *Pharmaceutics* 2020;**12**:371.

69. Donahue ND, Acar H, Wilhelm S. Concepts of nanoparticle cellular uptake, intracellular trafficking, and kinetics in nanomedicine. *Adv Drug Deliv Rev* 2019;**143**:68−96.

70. Kadlecova Z, Spielman SJ, Loerke D, Mohanakrishnan A, Reed DK, Schmid SL. Regulation of clathrin-mediated endocytosis by hierarchical allosteric activation of AP$_2$. *J Cell Biol* 2017;**216**:167−79.

71. Zhang F, Guo H, Zhang J, Chen Q, Fang Q. Identification of the caveolae/raft-mediated endocytosis as the primary entry pathway for aquareovirus. *Virology* 2018;**513**:195−207.

72. Vercauteren D, Vandenbroucke RE, Jones AT, Rejman J, Demeester J, De Smedt SC, et al. The use of inhibitors to study endocytic pathways of gene carriers: optimization and pitfalls. *Mol Ther* 2010;**18**:561−9.

73. Varkouhi AK, Scholte M, Storm G, Haisma HJ. Endosomal escape pathways for delivery of biologicals. *J Contr Release* 2011;**151**: 220−8.

74. Liu P, Sun Y, Wang Q, Sun Y, Li H, Duan Y. Intracellular trafficking and cellular uptake mechanism of mPEG-PLGA-PLL and mPEG-PLGA-PLL-Gal nanoparticles for targeted delivery to hepatomas. *Biomaterials* 2014;**35**:760−70.

75. Devadas D, Koithan T, Diestel R, Prank U, Sodeik B, Dohner K. Herpes simplex virus internalization into epithelial cells requires Na$^+$/H$^+$ exchangers and p21-activated kinases but neither clathrin-nor caveolin-mediated endocytosis. *J Virol* 2014;**88**:13378−95.

76. Martinez-Outschoorn UE, Sotgia F, Lisanti MP. Caveolae and signalling in cancer. *Nat Rev Cancer* 2015;**15**:225−37.

77. Parton RG, Simons K. The multiple faces of caveolae. *Nat Rev Mol Cell Biol* 2007;**8**:185−94.

78. Sahay G, Kim JO, Kabanov AV, Bronich TK. The exploitation of differential endocytic pathways in normal and tumor cells in the selective targeting of nanoparticulate chemotherapeutic agents. *Biomaterials* 2010;**31**:923−33.

79. Yang D, Liu D, Deng H, Zhang J, Qin M, Yuan L, et al. Transferrin functionization elevates transcytosis of nanogranules across epithelium by triggering polarity-associated transport flow and positive cellular feedback loop. *ACS Nano* 2019;**13**:5058−76.

80. Inpanathan S, Botelho RJ. The lysosome signaling platform: adapting with the times. *Front Cell Dev Biol* 2019;**7**:113.

81. Button RW, Roberts SL, Willis TL, Hanemann CO, Luo S. Accumulation of autophagosomes confers cytotoxicity. *J Biol Chem* 2017; **292**:13599−614.

82. Watanabe E, Muenzer JT, Hawkins WG, Davis CG, Dixon DJ, McDunn JE, et al. Sepsis induces extensive autophagic vacuolization in hepatocytes: a clinical and laboratory-based study. *Lab Invest* 2009;**89**:549−61.

83. Salazar M, Hernandez-Tiedra S, Torres S, Lorente M, Guzman M, Velasco G. Detecting autophagy in response to ER stress signals in cancer. *Methods Enzymol* 2011;**489**:297−317.

84. Higgins CM, Jung C, Xu Z. ALS-associated mutant SOD1G93A causes mitochondrial vacuolation by expansion of the intermembrane space and by involvement of SOD1 aggregation and peroxisomes. *BMC Neurosci* 2003;**4**:16.

85. Nakajima A, Kurihara H, Yagita H, Okumura K, Nakano H. Mitochondrial extrusion through the cytoplasmic vacuoles during cell death. *J Biol Chem* 2008;**283**:24128−35.

86. Chen S, Jiang YZ, Huang L, Zhou RJ, Yu KD, Liu Y, et al. The residual tumor autophagy marker LC3B serves as a prognostic marker in local advanced breast cancer after neoadjuvant chemotherapy. *Clin Cancer Res* 2013;**19**:6853−62.

87. Satyavarapu EM, Das R, Mandal C, Mukhopadhyay A, Mandal C. Autophagy-independent induction of LC3B through oxidative stress reveals its non-canonical role in anoikis of ovarian cancer cells. *Cell Death Dis* 2018;**9**:934.

88. Wang S, Tao J, Chen H, Kandadi MR, Sun M, Xu H, et al. Ablation of AKT2 and AMPK*α*2 rescues high fat diet-induced obesity and

hepatic steatosis through Parkin-mediated mitophagy. *Acta Pharm Sin B* 2021;**11**:3508−26.

89. Eiyama A, Okamoto K. Pink1/Parkin-mediated mitophagy in mammalian cells. *Curr Opin Cell Biol* 2015;**33**:95−101.

90. Iguchi M, Kujuro Y, Okatsu K, Koyano F, Kosako H, Kimura M, et al. Parkin-catalyzed ubiquitin-ester transfer is triggered by PINK1-dependent phosphorylation. *J Biol Chem* 2013;**288**:22019−32.

91. Li YF, Ouyang SH, Tu LF, Wang X, Yuan WL, Wang GE, et al. Caffeine protects skin from oxidative stress-induced senescence through the activation of autophagy. *Theranostics* 2018;**8**:5713−30.

92. Yuan Y, Zheng Y, Zhang X, Chen Y, Wu X, Wu J, et al. BNIP3L/-NIX-mediated mitophagy protects against ischemic brain injury independent of PARK$_2$. *Autophagy* 2017;**13**:1754−66.

93. Zhu J, Dagda RK, Chu CT. Monitoring mitophagy in neuronal cell cultures. *Methods Mol Biol* 2011;**793**:325−39.

94. Wang J, Chen M, Wang M, Zhao W, Zhang C, Liu X, et al. The novel ER stress inducer Sec C triggers apoptosis by sulfating ER cysteine residues and degrading YAP *via* ER stress in pancreatic cancer cells. *Acta Pharm Sin B* 2022;**12**:210−27.

95. Sisinni L, Pietrafesa M, Lepore S, Maddalena F, Condelli V, Esposito F, et al. Endoplasmic reticulum stress and unfolded protein response in breast cancer: the balance between apoptosis and autophagy and its role in drug resistance. *Int J Mol Sci* 2019;**20**:857.

96. Siwecka N, Rozpedek W, Pytel D, Wawrzynkiewicz A, Dziki A, Dziki L, et al. Dual role of endoplasmic reticulum stress-mediated unfolded protein response signaling pathway in carcinogenesis. *Int J Mol Sci* 2019;**20**:4354.

97. Cybulsky AV. Endoplasmic reticulum stress, the unfolded protein response and autophagy in kidney diseases. *Nat Rev Nephrol* 2017;**13**:681−96.

98. Wei Y, Pattingre S, Sinha S, Bassik M, Levine B. JNK1-mediated phosphorylation of BCL-2 regulates starvation-induced autophagy. *Mol Cell* 2008;**30**:678−88.

99. Huang T, Xu T, Wang Y, Zhou Y, Yu D, Wang Z, et al. Cannabidiol inhibits human glioma by induction of lethal mitophagy through activating TRPV$_4$. *Autophagy* 2021;**17**:3592−606.

100. Hu J, Wu Q, Wang Z, Hong J, Chen R, Li B, et al. Inhibition of CACNA$_1$H attenuates doxorubicin-induced acute cardiotoxicity by affecting endoplasmic reticulum stress. *Biomed Pharmacother* 2019;**120**:109475.

101. Wang J, Zhao H, Yu J, Xu X, Jing H, Li N, et al. MiR-320b/RAD$_{21}$ axis affects hepatocellular carcinoma radiosensitivity to ionizing radiation treatment through DNA damage repair signaling. *Cancer Sci* 2021;**112**:575−88.

102. Li C, Zhang Y, Liu J, Kang R, Klionsky DJ, Tang D. Mitochondrial DNA stress triggers autophagy-dependent ferroptotic death. *Autophagy* 2021;**17**:948−60.

103. Gredilla R, Garm C, Stevnsner T. Nuclear and mitochondrial DNA repair in selected eukaryotic aging model systems. *Oxid Med Cell Longev* 2012;**2012**:282438.

104. Zhu L, Sun C, Ren J, Wang G, Ma R, Sun L, et al. Stress-induced precocious aging in PD-patient iPSC-derived NSCs may underlie the pathophysiology of Parkinson's disease. *Cell Death Dis* 2019;**10**:105.

105. Kaarniranta K, Pawlowska E, Szczepanska J, Jablkowska A, Blasiak J. Role of mitochondrial DNA damage in ROS-mediated pathogenesis of age-related macular degeneration (AMD). *Int J Mol Sci* 2019;**20**:2374.

106. Yan C, Duanmu X, Zeng L, Liu B, Song Z. Mitochondrial DNA: distribution, mutations, and elimination. *Cells* 2019;**8**:379.

107. Jeng JY, Yeh TS, Lee JW, Lin SH, Fong TH, Hsieh RH. Maintenance of mitochondrial DNA copy number and expression are essential for preservation of mitochondrial function and cell growth. *J Cell Biochem* 2008;**103**:347−57.

108. Li C, Zhang Y, Liu J, Kang R, Klionsky DJ, Tang D. Mitochondrial DNA stress triggers autophagy-dependent ferroptotic death. *Autophagy* 2020;**17**:948−60.

109. Longchamps RJ, Castellani CA, Yang SY, Newcomb CE, Sumpter JA, Lane J, et al. Evaluation of mitochondrial DNA copy number estimation techniques. *PLoS One* 2020;**15**:e0228166.

110. Lan L, Guo M, Ai Y, Chen F, Zhang Y, Xia L, et al. Tetramethylpyrazine blocks TFAM degradation and up-regulates mitochondrial DNA copy number by interacting with TFAM. *Biosci Rep* 2017;**37**:BSR20170319.

111. Allkanjari K, Baldock RA. Beyond base excision repair: an evolving picture of mitochondrial DNA repair. *Biosci Rep* 2021;**41**:BSR20211320.

112. Kopinski PK, Singh LN, Zhang S, Lott MT, Wallace DC. Mitochondrial DNA variation and cancer. *Nat Rev Cancer* 2021;**21**:431−45.

113. Wu Z, Sainz AG, Shadel GS. Mitochondrial DNA: cellular genotoxic stress sentinel. *Trends Biochem Sci* 2021;**46**:812−21.

114. Matsushima Y, Goto Y, Kaguni LS. Mitochondrial lon protease regulates mitochondrial DNA copy number and transcription by selective degradation of mitochondrial transcription factor a (TFAM). *Proc Natl Acad Sci U S A* 2010;**107**:18410−5.

115. Besse A, Brezavar D, Hanson J, Larson A, Bonnen PE. LONP1 *de novo* dominant mutation causes mitochondrial encephalopathy with loss of LONP1 chaperone activity and excessive LONP1 proteolytic activity. *Mitochondrion* 2020;**51**:68−78.

116. Tian Q, Li T, Hou W, Zheng J, Schrum LW, Bonkovsky HL. Lon peptidase 1 (LONP1)-dependent breakdown of mitochondrial 5-aminolevulinic acid synthase protein by heme in human liver cells. *J Biol Chem* 2011;**286**:26424−30.

117. Quiros PM, Espanol Y, Acin-Perez R, Rodriguez F, Barcena C, Watanabe K, et al. ATP-dependent lon protease controls tumor bioenergetics by reprogramming mitochondrial activity. *Cell Rep* 2014;**8**:542−56.

118. Bota DA, Davies KJ. Mitochondrial Lon protease in human disease and aging: including an etiologic classification of Lon-related diseases and disorders. *Free Radic Biol Med* 2016;**100**:188−98.

119. Gibellini L, De Gaetano A, Mandrioli M, Van Tongeren E, Bortolotti CA, Cossarizza A, et al. The biology of Lonp1: more than a mitochondrial protease. *Int Rev Cell Mol Biol* 2020;**354**:1−61.

120. Liu T, Lu B, Lee I, Ondrovicova G, Kutejova E, Suzuki CK. DNA and RNA binding by the mitochondrial lon protease is regulated by nucleotide and protein substrate. *J Biol Chem* 2004;**279**:13902−10.

121. Chiu SJ, Lee YJ, Hsu TS, Chen WS. Oxaliplatin-induced gamma-H$_2$AX activation *via* both p53-dependent and -independent pathways but is not associated with cell cycle arrest in human colorectal cancer cells. *Chem Biol Interact* 2009;**182**:173−82.

122. Shi J, Kantoff PW, Wooster R, Farokhzad OC. Cancer nanomedicine: progress, challenges and opportunities. *Nat Rev Cancer* 2017;**17**:20−37.

123. Kou L, Sun J, Zhai Y, He Z. The endocytosis and intracellular fate of nanomedicines: implication for rational design. *Asian J Pharm Sci* 2013;**8**:1−10.